

THESIS FOR THE DEGREE OF DOCTOR OF PHILOSOPHY

Reactions on nanostructured and microporous surfaces

Anna Clemens



Department of Applied Physics

CHALMERS UNIVERSITY OF TECHNOLOGY

Göteborg, Sweden 2015

Reactions on nanostructured and microporous surfaces
Anna Clemens

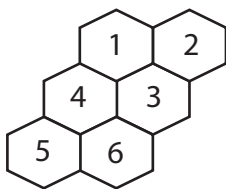
© Anna Clemens, 2015.

ISBN 978-91-7597-297-8

Doktorsavhandlingar vid Chalmers tekniska högskola
Ny serie Nr 3978
ISSN 0346-718X

Department of Applied Physics
Chalmers University of Technology
SE-412 96 Göteborg
Sweden
Telephone + 46 (0)31-772 1000

Cover illustration



1. STEM images of Cu-CHA before and after $[\text{NH}_3+\text{NO}]$ -SSIE.
2. NO-DRIFT spectra of Cu-CHA.
3. Activity of Cu-CHA for NH_3 -SCR.
4. Reflected light intensity and MS signal during thermal desorption of water from the NGS.
5. Schematic of water desorbing from the NGS.
6. View on the NGS sample through a window of the UHV chamber during illumination.

Printed at Chalmers Reproservice
Göteborg, Sweden 2015

Reactions on nanostructured and microporous surfaces

Anna Clemens

Department of Applied Physics

Chalmers University of Technology

Abstract

Interactions between surfaces and molecules play a central role in various fields where catalysis is one example. In order to understand different surface processes, physicochemical characterisation of the surface materials and molecules is required. The present work aims at characterisation of such processes on nanostructured and microporous surfaces with application for astrochemistry and selective NO_x reduction.

The astrochemical studies are motivated by the need for realistic model systems of interstellar dust grains that serve as catalysts for the formation of molecules in the interstellar medium. Experimentally, interstellar dust grains are commonly modelled by flat metal surfaces, although such structures are far from reality. This can result in inaccurate predictions of the surface processes, and thus, the molecular abundances in different regions in space. Temperature programmed desorption (TPD) with quadrupole mass spectrometry (QMS) at ultra-high vacuum conditions and optical reflection spectroscopy are used to study the thermal desorption of water from an ice-covered nanostructured graphite surface. It is found that the nanostructured surface gives rise to the presence of multiple peaks in TPD-QMS spectra, which can be assigned to water bound in two- and three-dimensional hydrogen-bonded networks, defect-bound water, and to water intercalated in the graphite structures. The diffusely reflected light from the surface measured during a TPD experiment is found to be dependent on the water ice phase and thickness, allowing the observation of water ice also in subsurface regions.

In emission control for automotive applications, there is a requirement for catalysts that are active for the conversion of nitrogen oxides (NO_x) to harmless N_2 over a broad temperature range. One of the most common approaches for heavy-duty vehicles is selective catalytic reduction with ammonia as reducing agent (NH_3 -SCR) over copper-exchanged zeolites. However, for cold exhausts, the catalytic activity of the copper zeolites is not sufficient and a deeper understanding of the detailed reaction mechanism and the properties of the catalytically active centres are required to further improve the technique. In this work, the properties of copper-containing chabazite (Cu-CHA) zeolites are investigated. The samples are prepared using both high-temperature solid-state ion-exchange (SSIE) in air and low-temperature SSIE performed in a reactive gas atmosphere containing NH_3 and NO. The Cu-CHA samples are characterised by infrared, optical and X-ray photoelectron spectroscopy together with X-ray diffraction, electron microscopy, and TPD of NH_3 and NO. In addition, the catalytic activity for the NH_3 -SCR reaction is investigated. It is observed that Cu ions from external CuO diffuse into the microporous structure of the zeolite under NH_3 -SCR conditions as well as in the presence of NH_3 and NO. Materials prepared by low-temperature SSIE assisted by NH_3 and NO show the highest conversion of NO_x for NH_3 -SCR with a maintained selectivity for N_2 formation. In both types of Cu-CHA materials, the presence of Cu^{2+} and Cu^+ species is suggested as a result of the SSIE procedures.

Keywords: Water ice, nanostructured graphite, ultra-high vacuum, temperature programmed desorption, intercalation, catalysis, NH_3 -SCR, NO_x reduction, zeolites, Cu-SSZ-13, Cu-CHA, solid-state ion-exchange, UV-Vis spectroscopy, XPS, DRIFTS, XRD, electron microscopy, materials characterisation

List of Publications

This thesis is based on the work presented in the following publications:

Paper I

Water Desorption from Nanostructured Graphite Surfaces

Anna Clemens, Lars Hellberg, Henrik Grönbeck and Dinko Chakarov
Physical Chemistry Chemical Physics, 15, 20456–20462 (2013)

Paper II

Reaction-driven Ion Exchange of Copper into Zeolite SSZ-13

Anna K. S. Clemens, Alexander Shishkin, Per-Anders Carlsson,
Magnus Skoglundh, Francisco J. Martínez-Casado, Zdenek Matěj,
Olivier Balmes and Hanna Härelind
ACS Catalysis, 5, 6209–6218 (2015)

Paper III

Highly Active Cu-CHA NH_3 -SCR Catalysts Prepared by Solid-State Ion-Exchange Facilitated by NH_3 and NO

Alexander Shishkin, Soran Shwan, Anna K. S. Clemens, Hanna Härelind, Per-Anders Carlsson, Torben Pingel, Eva Olsson and Magnus Skoglundh
Submitted to Applied Catalysis B: Environmental

Paper IV

Probing Copper Species in Solid-State Ion-Exchanged Cu-CHA by Selective Chemisorption of CO and NO

Anna K. S. Clemens, Alexander Shishkin, Per-Anders Carlsson,
Magnus Skoglundh and Hanna Härelind
Submitted to Journal of Physical Chemistry C

Related publications not included in the thesis:

Selective Catalytic Reduction with Ammonia over Double-Exchanged Cu-Fe-BEA Catalysts: Excellent Activity over Wide Temperature Range

Soran Shwan, Alexander Shishkin, Torben Pingel, Eva Olsson, Anna K. S. Clemens, Per-Anders Carlsson, Hanna Härelind and Magnus Skoglundh
In manuscript

Direct Synthesis of Boron-Substituted CHA Framework Structure

Alexander Shishkin, Anna K. S. Clemens, Francisco J. Martínez-Casado, L. Bock, Alexander Idström, Lars Nordstierna, Hanna Härelind, Per-Anders Carlsson, Magnus Skoglundh
In manuscript

My contributions to the appended papers

Paper I

Conducted the experiments, performed the data analysis and wrote the first draft of the paper.

Paper II

Prepared the samples, conducted the experiments except for the high-resolution XRD measurements, performed the data analysis and wrote the first draft of the paper.

Paper III

Participated in the experiments, the data analysis and the writing of the paper.

Paper IV

Prepared the majority of the samples, conducted the experiments, performed the data analysis and wrote the first draft of the paper.

Contents

1	Introduction	1
1.1	Astrochemistry	2
1.2	Selective NO _x Reduction	5
1.3	The Surface Science Approach in Catalysis	7
1.4	Objectives of this Work	7
2	Elementary Surface Reactions	9
2.1	Principle of Catalysis	9
2.2	Adsorption	10
2.2.1	Adsorption Kinetics	11
2.2.2	Film Growth	12
2.3	Desorption	12
2.4	Diffusion	14
3	Model System of Interstellar Dust Grains	17
3.1	Properties of Graphite	18
3.2	Graphite Nanostructures	19
3.3	Water and Water Ice	20
3.4	Water-Graphite Interactions	21

3.4.1	Graphite Intercalation	22
4	Zeolite Catalysts	23
4.1	Properties and Synthesis of Zeolites	23
4.2	Metal Ion-Exchange in Zeolites	25
4.3	NH ₃ -SCR Mechanism over Cu-CHA	26
5	Characterisation Techniques	31
5.1	Experimental Setups	31
5.1.1	Ultra-High Vacuum System	31
5.1.2	Flow Reactor System	33
5.2	Microscopy	33
5.3	Temperature Programmed Desorption (TPD)	35
5.4	Spectroscopy	39
5.4.1	UV-vis Spectroscopy	40
5.4.2	Infrared Spectroscopy	44
5.4.3	X-ray Diffraction	47
5.4.4	X-ray Photoelectron and Auger Electron Spectroscopy	48
6	Results and Discussion	51
6.1	Characterisation of Materials Properties	51
6.2	Interactions between Molecules and Surfaces	54
6.2.1	Temperature Programmed Desorption Results	54
6.2.2	Spectroscopy Results	55
6.3	Catalytic Surface Reactions	58
7	Conclusions and Outlook	61
	Acknowledgements	65
	Bibliography	67

List of Acronyms

2D/3D	Two-/Three-dimensional
AES	Auger electron spectroscopy
AFM	Atomic force microscopy
AIE	Aqueous ion-exchange
ASW	Amorphous solid water
BE	Binding energy
CHA	Chabazite
deNO_x	Removal of nitrogen oxides
DFT	Density functional theory
DPF	Diesel particulate filter
DRIFTS	Diffuse reflectance infrared Fourier transform spectroscopy
EDX	Energy-dispersive X-ray spectroscopy
EPR	Electron paramagnetic resonance
EXAFS	Extended X-ray absorption fine structure
HCL	Hole-mask colloidal lithography
HOPG	Highly oriented pyrolytic graphite
I_c	Crystalline ice
I_h	Hexagonal ice
(FT-)IR	Fourier transform-infrared
ISM	Interstellar medium
KE	Kinetic energy
LED	Light emitting diode
LEED	Low-energy electron diffraction
MFC	Mass flow controller
(Q)MS	(Quadrupole) mass spectrometry
NGS	Nanostructured graphite surface
[NH₃+NO]-SSIE	Solid-state ion-exchange in NH ₃ /NO atmosphere
(NH₃-) SCR	(Ammonia) selective catalytic reduction
S(T)EM	Scanning (transmission) electron microscopy

SSIE	Solid-state ion-exchange
SSZ-13	Synthetic zeolite with chabazite structure
TPD	Temperature programmed desorption
UHV	Ultrahigh vacuum
UV(-vis)	Ultraviolet(-visible)
XANES	X-ray absorption near edge structure
XPS	X-ray photoelectron spectroscopy
XRD	X-ray diffraction

Reactions occurring on complex surfaces play a major role in various fields of chemistry and physics where a dominant example is heterogeneous catalysis. A catalyst is a substance which accelerates a chemical reaction without being consumed itself [1]. In a heterogeneously catalysed reaction, the phase of the catalyst is different from that of the reactants, *e.g.* a solid catalyst surface in a gaseous reactant mixture. Heterogeneous catalysis is essential for the production of transportation fuels, bulk and fine chemicals, and the abatement of pollutants from automotive and industrial exhausts [1, 2]. However, catalytic processes are not only utilised in our modern world but also occur on interstellar dust grain particles in space and are responsible for the formation of molecules. This thesis considers two areas where complex, nanostructured and microporous, surfaces are used to study physicochemical processes and transformations. More specifically, in the area of astrochemistry, studies on nanostructured surfaces composed of carbon materials are needed in order to construct more realistic model systems for interstellar dust grains. In the field of selective NO_x reduction, there is a great need for characterisation of microporous zeolite materials that are applied as catalysts aiming at a greater understanding of the catalytic reactions used to clean exhaust gases from pollutants.

In this Chapter, a background to both astrochemistry and selective NO_x reduction will be given.

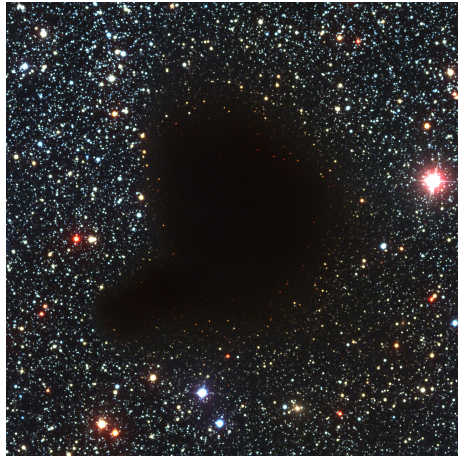


Figure 1.1: The “Black Cloud” Barnard 68. This figure is obtained from ESO (<http://www.eso.org/public/images/eso9924a/>).

1.1 Astrochemistry

Despite the very low pressure in space, the regions between the stars, the interstellar medium (ISM), is not empty. Instead, it is filled with a large variety of gases, ices, and solid particles. The presence of solid particles, referred to as interstellar dust grains, has a considerable impact on the molecular composition in the ISM because of physical and chemical processes that occur on the grain surfaces [3]. At present, almost 200 different molecules have been identified in the interstellar medium or circumstellar shells [4], and water (H_2O) is one of them [5]. Molecules can form in the ISM by gas-phase reactions induced by *e.g.* cosmic rays or by surface reactions on interstellar dust grains. Indeed, the enhanced abundances of some gas-phase molecules, such as H_2 [6, 7] and NH_3 [8], as well as the presence of alcohols, such as methanol [9, 10], is commonly explained by surface reactions on grains as no efficient gas-phase formation route is known.

Interstellar dust was probably noticed for the first time by the astronomer William Herschel in 1784 [11]. He was astonished by the presence of “holes in the sky”, *i.e.* apparent voids in the distribution of stars in the night sky, as shown in Figure 1.1. It is now known that such black regions in interstellar clouds are owing to dust particles that absorb and scatter and, hence, extinguish most of the visible light from stars that are present in the background.

Interstellar dust grains are in many cases composed of a grain core and an icy grain mantle, as shown on the left panel in Figure 1.2. The interstellar ices in the grain mantle form by condensation of gas phase molecules on cold

dust grain surfaces. The molecular composition of interstellar grains can be derived from astronomical infrared absorption spectra. An example is shown on the right panel in Figure 1.2. The spectrum shows the presence of several molecules in the icy grain mantle, as well as the dust grain core material, in this case a silicate. By far, the most abundant molecule in ice mantles is water, detectable through the broad absorption band at around $3\ \mu\text{m}$ that originates from the OH stretching of water ice in an amorphous phase. Other frequent molecules are CO, CO₂, CH₃OH, H₂CO, HCOOH, NH₃ and CH₄, but their abundances are often below 20% relative to the water abundance.

Apart from silicates, dust grain cores can consist of carbonaceous materials and also heavier elements, such as Al, Ti and Fe [3]. The carbonaceous components in dust grains are mainly dominated by graphitic and amorphous carbon. The profile of the strong interstellar absorption feature at 217.5 nm points to the existence of nanosized carbonaceous structures [12, 13]. This was concluded because of the high similarity of the spectral characteristics of defective carbon nanostructures [12] and amorphous carbon nanoparticles [13] with the astronomical band profiles. Furthermore, observed shifts of the weak interstellar bands at 6.8 and 7.2 μm have been interpreted as the presence of defective nanostructures in carbonaceous dust [14]. Dust grain sizes can be derived from optical extinction curves because the wavelength of the extinction is dependent on the grain size. They can span a wide range, from a few to several hundred nanometres [3]. The sizes and structures of interstellar grains are highly influenced by the extreme conditions in space, in particular the temperature, that may range from 10 to 10^6 K depending on the region, as well as ultraviolet (UV), X-ray or cosmic radiation, consisting of high energy protons and electrons. Therefore, the surface of interstellar grains is assumed to be inhomogeneous. Exposure to the different forms of radiation and elevated temperatures can furthermore lead to changes in the ice morphology. It can also result in chemical reactions and the formation of new species, especially more complex organic molecules [15–17]. Finally, at sufficiently high energies, interstellar ices can desorb thermally or under the influence of UV photons.

For an accurate interpretation of astronomical observations, adequate model systems, also referred to as dust grain analogues, must be chosen. This enables the investigation of astrophysical or astrochemical processes that involve interstellar dust grain surfaces in the laboratory or by computer simulations. The advantage of dust grain analogues is that they can be examined at chosen conditions and with different techniques, *e.g.* under the influence of varying temperatures, or under the exposure to photons, electrons or ions. Modelling of interstellar processes in the laboratory can also result in remarkable discoveries. For example, the formation of the carbon allotrope C₆₀, known as buckminsterfullerene, was detected for the first time in 1985 by H. Kroto and coworkers during laser induced evaporation experiments of graphite [19].

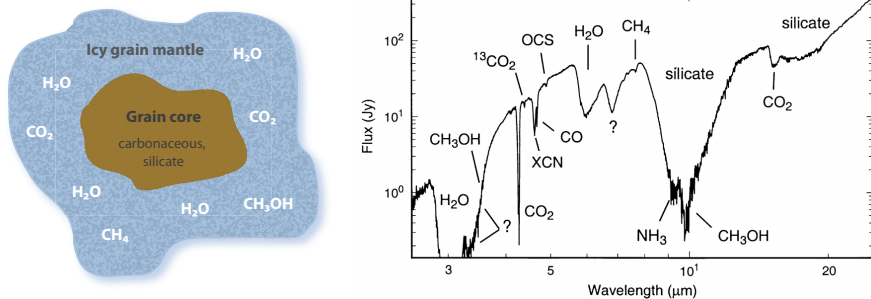


Figure 1.2: *Left panel: Schematic of an interstellar dust grain consisting of a grain core and an icy grain mantle; Right panel: Astronomically observed infrared absorption spectrum toward the molecular cloud W33A showing molecules that are present in the icy mantle (H_2O , CO_2 , CH_3OH , CH_4 , etc.) as well as the grain core material (silicate). Reproduced by the permission of the AAS from Gibb et al. [18].*

To accurately model star forming regions, a detailed understanding of thermal desorption processes is crucial. While the icy mantle on interstellar dust grains form in the cold, dense molecular clouds, they can sublimate during the lifetime of a molecular cloud (10^6 – 10^8 years) when newly formed stars warm up the grain material [3]. The warm and dense star-forming regions (called hot cores) typically contain the ice mantle molecules in gas-phase. Although assumed in many astrophysical models, the desorption of interstellar ices does not occur instantaneously when a star in the vicinity is switched on [20]. It has been shown that the models can be improved by using the experimentally obtained kinetic parameters of the thermal desorption processes [21].

It is clear, however, that laboratory astrochemical and astrophysical experiments have limitations as models for interstellar processes. For example, interstellar particle densities can be in the order of 200 cm^{-3} in molecular clouds, and around 1 – 10^5 cm^{-3} in regions where star formation has recently taken place [3]. In contrast, under laboratory conditions with ultra-high vacuum (UHV), pressures in the order of 10^{-11} torr can be reached. This corresponds to a particle density of approximately 10^7 cm^{-3} at 10 K, *i.e.* several orders of magnitude higher. Furthermore, heating rates in hot cores are approximated to 1 K per century (which is equivalent to approximately $3 \times 10^{-9}\text{ K s}^{-1}$) [20, 21] whereas, in the laboratory, heating rates on the order of 1 K s^{-1} are usually applied.

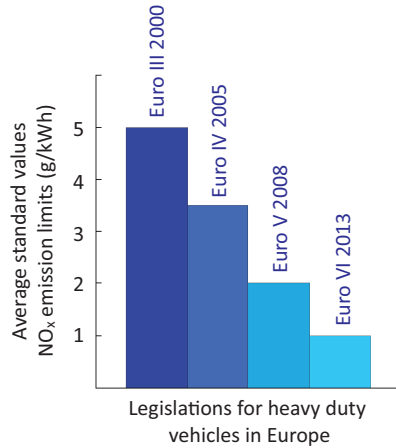


Figure 1.3: NO_x emission limits for heavy-duty vehicles according to the European legislations in the past 15 years. The data for this plot was taken from Ref. [25].

1.2 Selective NO_x Reduction

Exhaust emissions from automotive vehicles include nitrogen oxides (NO_x), carbon monoxide (CO), hydrocarbons (HC) and particulate matter [1]. This thesis focuses on the abatement of NO_x , which is a collective term used for nitric oxide (NO) and nitrogen dioxide (NO_2) [22], and is associated with severe environmental and health concerns [22–24]. In the atmosphere, NO_x can react to form smog and acid rain, as well as tropospheric ozone [22, 23]. Furthermore, it can lead to acidification and eutrophication, *i.e.* a nutrient enrichment of the Earth’s surface that has a destructive impact on both aquatic and terrestrial ecosystems [24]. In humans, NO_2 can lead to respiratory problems owing to the formation of nitrous and nitric acids with body moisture that can attack the walls of lung alveoli [22]. Therefore, the emission of NO_x gases has been subject to increasingly stringent legislation during the past decades, in particular in Europe, the United States of America, and Japan. As an example, the NO_x emission limits in Europe for diesel heavy-duty vehicles during the past 15 years are shown in Fig. 1.3. According to the Euro VI emission standards implemented in 2013, only 0.2–1.0 g/kWh NO_x are allowed to be released from heavy-duty vehicles within the European Union [25, 26].

In gasoline powered vehicles, NO_x emissions are commonly abated using a three-way catalytic converter. However, the three-way catalyst does not function at the high air/fuel ratios, *i.e.* at lean conditions, that most diesel engines operate on in order to be more fuel efficient. Therefore, other systems are required in diesel-powered vehicles for the removal of NO_x ($deNO_x$) working at highly oxidising conditions. The leading $deNO_x$ strategy in heavy-duty

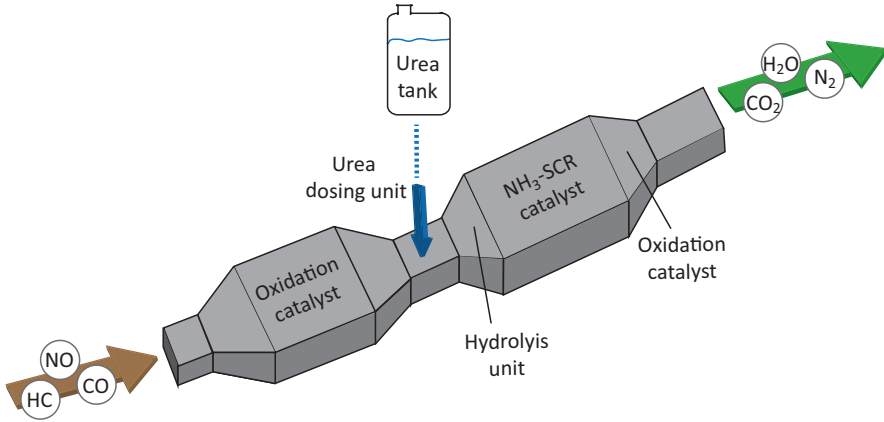
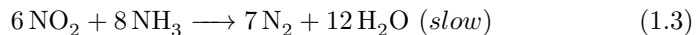
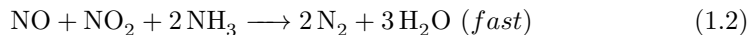
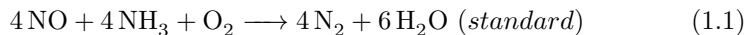


Figure 1.4: Scheme of a diesel aftertreatment system with an NH_3 -SCR catalyst for conversion of NO_x exhaust gases to N_2 .

vehicles is selective catalytic reduction with ammonia as the reducing agent (NH_3 -SCR) [27]. It is typically incorporated in a diesel aftertreatment system which is shown schematically in Fig. 1.4. The aftertreatment system consists of different parts, *i.e.* an oxidation unit, a urea system, a part for urea hydrolysis, an NH_3 -SCR catalyst, and a second oxidation catalyst [28]. Not shown in the scheme, but usually also part of a diesel aftertreatment system is the diesel particulate filter (DPF) for removal of particulate matter that can be integrated as a separate unit or as combined SCR-DPF system [29]. The catalysts used in the catalytic units are usually wash-coated on ceramic or stainless steel monoliths. Their honeycomb structure functions as the catalyst substrate, increasing the surface area exposed of the catalyst [1].

In the first oxidation unit, NO, CO and hydrocarbons (HC) are oxidised to form NO_2 and CO_2 , respectively. Through a dosing unit, urea is injected to the gas mixture. The urea is hydrolysed in situ to form ammonia (NH_3) which acts as the reducing agent in the SCR unit. Usually, NH_3 -SCR can proceed via the following three reduction reactions of nitrous oxide (NO) and/or nitrogen dioxide (NO_2) with ammonia under oxygen excess:



The notation of *fast* and *slow* NH_3 -SCR is derived from their proceeding at faster and slower reaction rates, respectively, compared to the *standard* NH_3 -

SCR reaction. In the last step of the exhaust aftertreatment, the remaining ammonia is oxidised over a second oxidation catalyst to form N_2 . This reaction is also a major side reaction of the NH_3 -SCR reaction as the direct ammonia oxidation by molecular oxygen bypasses the reduction of NO_x :



1.3 The Surface Science Approach in Catalysis

At first glance, astrochemistry and selective NO_x reduction may seem to be disconnected fields. However, the basic ingredient of both disciplines is heterogeneous catalysis, *i.e.* processes taking place on surfaces and, therefore, both fields rely on the same basic concepts of surface science. Their study requires similar knowledge about material properties, and the same characterisation techniques such as electron microscopy and spectroscopy are used. Furthermore, the interaction between adsorbing, desorbing and reacting molecules is probed to gain information about the surfaces as well as the processes occurring on the surfaces.

1.4 Objectives of this Work

The aim of this work is to investigate reactions that occur on nanostructured and microporous surfaces. In the astrochemistry studies, the influence of the surface morphology and other size-related properties of a nanostructured graphite surface on the thermal desorption of water is studied. The use of a graphitic and nanostructured substrate is motivated by the need for realistic model surfaces for studies of astrochemical and astrophysical processes on interstellar dust grains. An understanding of water desorption processes is essential for astrochemical modelling of surface processes because water is the major component in the interstellar ices that are deposited on dust grains. The nanostructured graphite samples are characterised by electron and atomic-force microscopy. The thermal desorption is studied by temperature programmed desorption (TPD) combined with detection by mass spectrometry (MS) and reflectance spectroscopy.

In the selective NO_x reduction investigation, the catalytic activity for NH_3 -SCR of copper-exchanged chabazite zeolites prepared by different methods of solid-state ion-exchange is investigated and the nature and oxidation state of the Cu species present in the samples are assessed. The motivation for these studies arises from the requirement for catalysts that are highly active

for the abatement of toxic exhaust gases over a broad temperature range. For sample characterisation, infrared, optical, X-ray photoelectron and Auger spectroscopy are used together with X-ray diffraction, electron microscopy and TPD of NH_3 and NO .

The thesis is structured as follows: In Chapter 2, an introduction to some fundamental surface processes will be given. In Chapter 3, previously studied dust grain analogue systems, and the properties of the interstellar dust grain model system used in the present studies will be described. In Chapter 4, the properties and preparation of metal-containing zeolite catalysts will be outlined and the state-of-the-art understanding of the reaction mechanism of NH_3 -SCR over copper chabazite catalysts will be summarised. Chapter 5 provides a presentation of the experimental methods, which are based on ultra-high vacuum techniques as well as methods at ambient conditions. In Chapter 6, a summary of the obtained results will be presented and in Chapter 7 conclusions will be drawn and an outlook for future work on this topic will be given.

Elementary Surface Reactions

This Chapter will give a general background to some fundamental concepts in surface science with a focus on topics that are relevant for the presented studies. Elementary surface reactions include adsorption, desorption, diffusion and reaction, as illustrated in Figure 2.1. These processes have been discussed in several textbooks, of which the book by K. W. Kolasinski is one example [2].

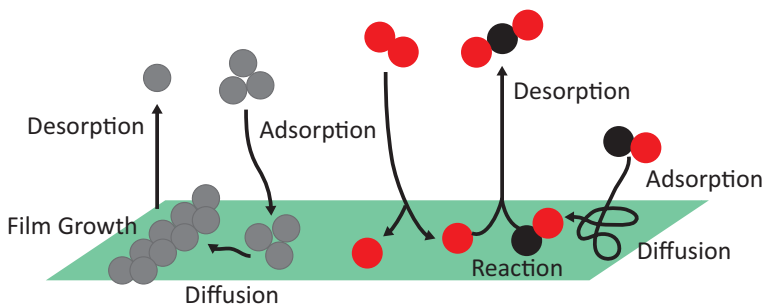


Figure 2.1: Schematic representation of elementary surface processes.

2.1 Principle of Catalysis

As illustrated in Fig. 2.2, the addition of a heterogeneous catalyst to a reaction provides a new reaction pathway to the uncatalysed (gas-phase) reaction [30]. The catalysed reaction exhibits lower activation energies (E_a^i) than the uncatalysed reaction (E_a), which leads to an increase in reaction rate.

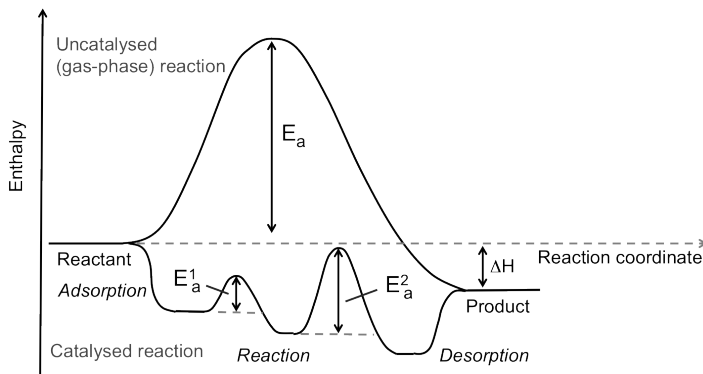


Figure 2.2: Reaction enthalpies of an uncatalysed and a catalysed reaction.

Note that the change in enthalpy, ΔH , is identical for both the catalysed and uncatalysed reaction meaning that the thermodynamics of the reaction are unchanged by addition of a catalyst, while the kinetics are affected [30].

2.2 Adsorption

The adsorption of molecules and atoms on solid surfaces is commonly divided into two types: physical adsorption, called *physisorption*, and chemical adsorption, called *chemisorption* [2]. The potential energy of the molecule or atom as it approaches the surface describes the interaction between an adsorbate and a surface. In Figure 2.3, examples of potential energy curves are given. The depth of the potential well, E_{ads} , represents the energy that is gained upon adsorption, the binding energy.

For a physisorbed adsorbate, the resulting potential well, denoted as $E_{\text{ads}}^{\text{phys}}$ in Figure 2.3, is comparably shallow, typical values are ≤ 0.3 eV [2]. Therefore, physisorption is considered as the weakest form of adsorption. It can be interpreted as a balance of a long-range van der Waals attraction, that involves a fluctuating polarisation of the adsorbate, and a short-range Pauli repulsion, originating from an unfavourable overlap of the filled atomic orbitals of the adsorbate with those of the surface atoms. Due to the low binding energy, physisorption is studied at low temperatures, usually ≤ 100 K.

In contrast, in the case of chemisorption, new ionic, covalent and/or metallic bonds between adsorbate and surface are formed owing to a constructive overlap of the atomic orbitals. Consequently, chemisorption results in a deeper potential energy minimum. This is visualised in Figure 2.3, where the binding energy of the chemisorbed system is indicated as $E_{\text{ads}}^{\text{chem}}$. Commonly, binding

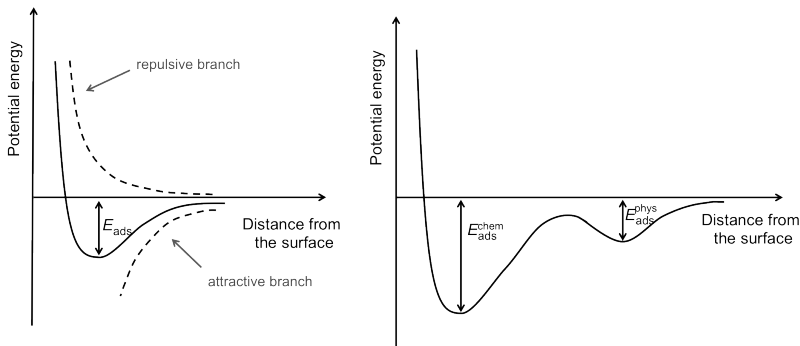


Figure 2.3: Examples of potential energy curves for a molecule or atom that is physisorbed or chemisorbed to a surface with adsorption energies $E_{\text{ads}}^{\text{phys}}$ and $E_{\text{ads}}^{\text{chem}}$, respectively.

energies of $\geq 1\text{ eV}$ are reported [2]. Chemisorption leads to strong perturbations of the molecular properties compared to those of the gas phase molecule. The bonding strength in chemisorbed systems is determined by the interaction between the valence electrons of the adsorbate and those of the solid surface. A special case is dissociative chemisorption, which involves breaking of the intramolecular bond of the adsorbed molecule and consequent atomic adsorption.

Lateral interactions between adsorbates can become crucial for the energetics of the adsorption process. These interactions are usually more important at high coverages. However, even at low coverages, lateral interactions can play a role, *e.g.* for island formation, *cf.* Section 2.2.2. Lateral interactions generally result in a coverage dependence of the adsorption energy [2].

2.2.1 Adsorption Kinetics

For a molecule to adsorb (stick) to a surface, it must lose enough energy to be trapped in the adsorption well at the surface. The sticking of molecules on a surface depends on the specific properties of both the substrate and the incident species, important factors to consider are the electronic structure, the temperature, and the angle of incidence. The sticking probability is described by the sticking coefficient S which is defined by the ratio of the number of particles that stick, N_{stick} , and the number of incident particles, N_{inc} :

$$S(\Theta, T_S) = \frac{N_{\text{stick}}}{N_{\text{inc}}} \quad (2.1)$$

where Θ is the adsorbate coverage, and T_S is the substrate temperature.

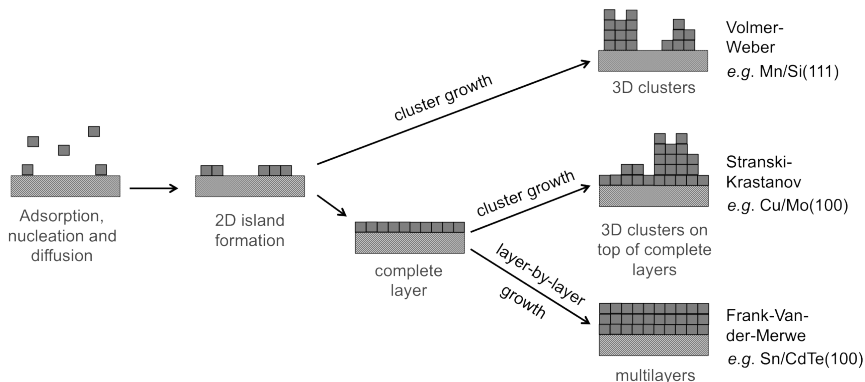


Figure 2.4: The different growth modes for molecules and atoms on a surface.

2.2.2 Film Growth

Experimental studies on various systems point to the existence of three different growth mechanisms for molecules and atoms on surfaces [31], as visualised in Figure 2.4. The growth of adsorbates on a surface begins with the adsorption of a small number of molecules that can diffuse on the surface until they find nucleation centers, *e.g.* defect sites on the substrate. With adsorption of more molecules, the formation of two-dimensional (2D) islands starts. The Volmer-Weber growth mechanism continues with the formation of three-dimensional (3D) clusters by adsorption of molecules on top of the 2D islands. In case of the Frank-Van-der-Merwe growth mode, first a complete monolayer is formed on the surface before the formation of the next layers starts in a layer-by-layer growth fashion. A mixture between these two growth modes is the Stranski-Krastanov mechanism, where cluster growth occurs after the formation of one or a few complete layers. The specific growth mechanism depends on the properties of the adsorbate and the surface, *e.g.* surface defects and lateral interactions can play an important role [31].

2.3 Desorption

Desorption is the inverse process of adsorption, and hence, energy is required to break the adsorbate-substrate bond. This energy can be transferred thermally or by incoming electrons or photons. In this thesis, desorption by thermal energy transfer is studied. Thermal desorption is driven by the exchange of vibrational energy from thermally excited states in the substrate (phonons) to the adsorbate. Increasing the temperature leads to a higher population of vibrationally excited states in the adsorbate-substrate bond and to a larger

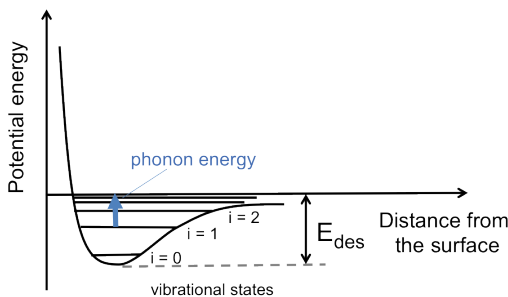


Figure 2.5: Schematic representation of the vibrational states of a physisorbed adsorbate, the blue arrow represents the required phonon energy for thermal desorption of the adsorbate to occur, and the desorption energy is marked as E_{des} .

number of high-energy phonons in the substrate, see Figure 5.9 [2]. The desorption of an adsorbate becomes more likely for highly excited vibrational states and phonons of high energies.

At thermal equilibrium between substrate and adsorbate, the desorption rate of Θ adsorbed species can be expressed in terms of an Arrhenius expression:

$$r_{des} = \frac{d\Theta}{dt} = A\Theta^n \exp\left(-\frac{E_{des}(\Theta)}{k_B T}\right) \quad (2.2)$$

where t is the time, E_{des} is the desorption energy, k_B the Boltzmann constant, T the substrate temperature, n the desorption order and A the pre-exponential factor. The physical meaning of the pre-exponential factor can be derived from transition state theory and the value of A can be understood as being determined by the looseness of the transition state relative to the adsorbed state of the desorbing species [2]. Typical values of A span between 10^{11} and 10^{19} s^{-1} .

Lateral interactions between the adsorbates influence the desorption in a similar way as the adsorption process, and impact the coverage dependence of the desorption rate and energy. For multilayer coverages, the desorption energy might be constant, whereas it might be coverage-dependent at sub-monolayer coverages.

For further reading, it is referred to Section 5.3, where the kinetics and energetics of the desorption process are described in more detail.

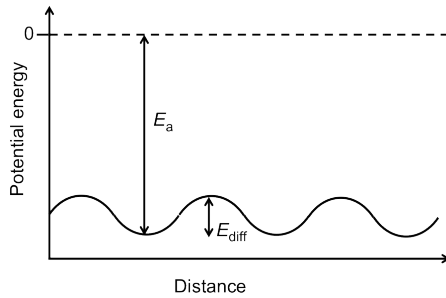


Figure 2.6: One-dimensional representation of the potential energy surface as a function of position on an ideal defect-free surface for a single adsorbate, illustrating the diffusion barriers. E_{ads} is the adsorption energy (see Figure 2.3) and E_{diff} is the activation energy for diffusion.

2.4 Diffusion

An ideal, defect-free surface exhibits many sites of the same type that the adsorbate can bind to. If sufficient vibrational energy is transferred to the system, lateral movement of the adsorbate across the surface can take place. This motion is referred to as surface *diffusion*. It is dependent on the energetic barriers between the different binding sites, called diffusion barriers.

Diffusion can be expressed in terms of an Arrhenius equation:

$$D = D_0 \exp\left(-\frac{E_{\text{diff}}}{k_B T}\right) \quad (2.3)$$

Here, D is the diffusion coefficient with dimensions of $[\text{length}^2 \text{ time}^{-1}]$, D_0 is the pre-exponential factor for diffusion, and E_{diff} the activation energy for diffusion. Because E_{diff} is typically only around 5-20% of the desorption energy [31], diffusion can usually take place at lower temperatures than the desorption.

Diffusion barriers can be represented by a one-dimensional potential energy surface. Figure 2.6 shows the potential energy of an adsorbate on an ideal defect-free surface. The depth of each well corresponds to the binding energy of the adsorbate to the surface, as discussed in Section 2.2. The height of the hills represents E_{diff} . For inhomogeneous substrates that exhibit a variety of binding sites and defects, as used in this study, the diffusion barriers vary in height.

Also for diffusion processes, lateral interactions between the adsorbates can play an important role [32]. Repulsive interactions between the adsorbates can

decrease the value of E_{diff} and increase the value of D . In contrast, attractive interactions can increase the value of E_{diff} while decreasing D , as in the case of water, which forms intermolecular hydrogen bonds.

Another thermally activated process is *absorption*, the diffusion of the adsorbate into subsurface regions of the substrate. For substrates with a layered structure, such as graphite, a special absorption phenomenon called *intercalation* can occur, where adsorbates can enter between the atomic layers. A more detailed description of graphite intercalation will be given in Section 3.4.1.

Model System of Interstellar Dust Grains

In order to investigate the thermal desorption of interstellar ices from dust grains in laboratory experiments or in computer simulations, suitable dust grain models must be developed. Based on knowledge from the well-established area of surface science, metal surfaces are generally used as models for dust grain surfaces. Examples include studies on gold [33–37] or platinum surfaces [38]. However, the desorption behaviour of a molecule can be dependent on the grain surface [39]. Hence, in order to model the thermal desorption of interstellar ices in a more realistic manner, graphite surfaces have also been used as dust grain models [40–44]. Furthermore, the influence of the surface morphology on the desorption of ices has recently begun to be investigated [45, 46]. In a study by Noble *et al.* [46], a strong dependence on the surface type and morphology was observed in thermal desorption experiments of CO, O₂ and CO₂. The influence of a porous and rough structure of an amorphous silica substrate on the thermal desorption of benzene was investigated by Thrower *et al.* [45], who found that the desorption energy and the pre-exponential factor vary with the coverage. One attempt to synthesise a realistic grain model surface was performed by Mautner and coworkers [47]. In that study, nanoparticles were produced by laser ablation and controlled condensation from a carbonaceous meteorite sample resulting in aggregates with porous web-like morphologies that resemble those found in interplanetary dust grains.

In this Chapter, the dust grain model system that was used in the astrochemical studies of this thesis will be introduced. The model system consists of a dust grain analogue surface that is composed of well-defined, nanometric, truncated cone structures of graphite, and water ice. First, the properties of

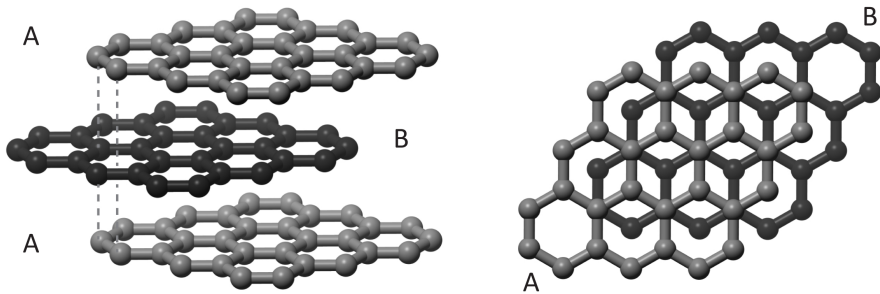


Figure 3.1: Graphite structure in side view (left panel) and top view (right panel) with ...ABA... stacking of the graphene layers.

graphite and the fabrication techniques of the nanostructured graphite surface will be described. Then, the characteristics of water and water ice will be presented. The interaction between graphite and water as well as graphite intercalation will be outlined at the end of the Chapter.

3.1 Properties of Graphite

Graphite is the most stable allotrope of carbon under standard conditions [48]. It has a planar, layered structure composed of basal planes, each of them called *graphene* if isolated. The structure of graphite is shown in Figure 3.1. Within each sheet, the sp^2 -hybridised carbon atoms are covalently bonded, forming a lattice with hexagonal symmetry with a C-C distance of 1.4 \AA . Each carbon atom forms three σ -bonds to the neighbouring atoms and the remaining valence electron is delocalised over the honeycomb structure in π -bonds. The sheets are stacked in an ...ABA... sequence with a separation of 3.4 \AA between the layers.

The difference in binding strengths within and between the graphite layers results in the characteristic anisotropic mechanical, electrical and thermal properties of graphite. The cleavage of graphite parallel to the layers is easy, and fresh graphite surfaces can be prepared by peeling off the top layers of a graphite sample with adhesive tape. Based on this method, K. Novoselov and A. Geim, Nobel Prize winners in Physics in 2010, invented a technique to prepare graphene [49]. In addition, graphite is a semiconductor and conducts electricity very well in the direction parallel to the basal planes due to the electron delocalization. In contrast, graphite is an insulator orthogonal to the graphene sheets.

Due to the weak interlayer bonds, graphite interacts very weakly with adsor-

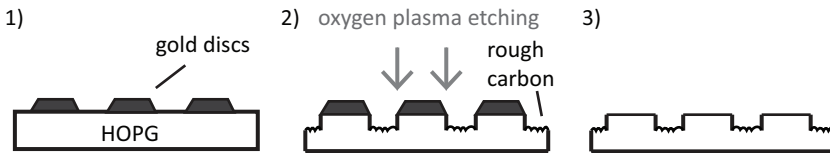


Figure 3.2: Scheme of the fabrication process of graphite nanostructures: 1) Preparation of gold nano-discs as masks on top of an HOPG surface, 2) Oxygen plasma etching to create graphite nanostructures and 3) Removal of the gold masks by chemical gold etching results in well-defined truncated cone structures of graphite covering a rough carbon surface.

bates. For the adsorption of most molecules, the presence of defects on the surface is therefore crucial. Water shows a non-wetting adsorption behaviour on graphite [43, 50, 51].

Highly oriented pyrolytic graphite (HOPG), that was used as starting material for dust grain model surfaces in this study, is a synthetic graphite material that exhibits a low defect density and highly anisotropic properties. It is synthesised by annealing of graphite under high pressure, resulting in an angular spread between the basal planes (mosaic spread) of $(0.4 \pm 0.1)^\circ$ for the highest quality HOPG [52].

3.2 Graphite Nanostructures

The well-defined graphite nanostructures used in this thesis can be fabricated from HOPG by oxygen plasma etching in combination with hole-mask colloidal lithography (HCL), a method developed by H. Fredriksson *et al.* [53, 54]. A schematic description of the fabrication process is shown in Figure 3.2. First, protecting gold nano-discs are prepared on top of HOPG by evaporation of gold onto a hole-mask made from a sacrificial polymer layer (a). Thereby, holes in the polymer layer determine the diameter of the gold discs. In the second step, the part of the HOPG surface that has not been protected by gold discs is removed by oxygen plasma etching (b). The surface between the structures is significantly roughened after the oxygen plasma etching. In the last step, after removal of the gold discs by a chemical gold etch, one obtains nanometric graphite structures in the shape of truncated cones of distinct height and diameter that decorate a rough carbon surface (c). The diameter of the graphite nanostructures is determined by the size of the masking gold discs, and the height is controlled by the conditions of the etching process.

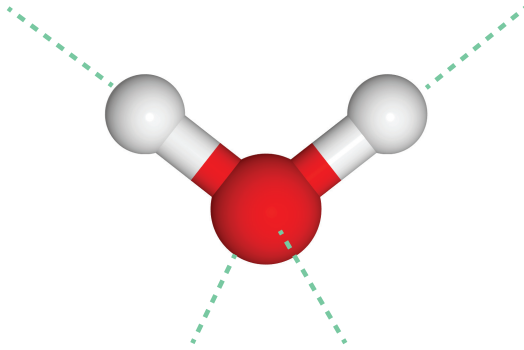


Figure 3.3: *The water molecule formed by two hydrogen (white) and one oxygen atom (red). Donor- and acceptor-sites to form hydrogen bonds are marked by dashed green lines.*

3.3 Water and Water Ice

A water (H_2O) molecule consists of an oxygen atom that is sp^3 -hybridised and covalently bound to two hydrogen atoms at an angle of 104.52° [55], as depicted in Figure 3.3. Water is a polar molecule due to its asymmetric distribution of electronic charge. Because of its two electron lone pairs, the oxygen atom can act as an H-bond acceptor, while the hydrogen atoms can act as H-bond donors. Thus, intermolecular attractive interactions between the hydrogen and oxygen atoms can be formed, so-called *hydrogen bonds*. The strength of a hydrogen bond in water is on the order of 0.1–0.3 eV/molecule [56], hence it is stronger than a van der Waals interaction but weaker than a covalent bond [57]. As a result of the intermolecular hydrogen bonding, water molecules can form dense *H-bond networks* by creating up to four hydrogen bonds per water molecule.

The solid phase of water, *ice*, can exist in a large variety of crystalline and amorphous phases with different morphologies. The phases are highly dependent on the preparation techniques and conditions, such as pressure and temperature. In the metastable amorphous phase, that constitutes the most abundant forms of water ice in interstellar space, the water molecules do not exhibit any long-range order [55]. To produce an amorphous solid of high density, low temperatures and high pressures are required. At very low temperatures and pressures, amorphous ices of low density can be obtained. When a surface with a temperature below $\sim 135\text{ K}$ is exposed to water in UHV, water ice grows in a low density amorphous phase called *amorphous solid water* (ASW) with varying morphologies depending on the experimental conditions, such as the deposition angle and the deposition rate [58–60]. ASW has an extremely large surface area owing to the presence of pores and cracks. A

transition to a supercooled liquid state occurs at a temperature of ~ 135 K, known as the glass transition temperature [61, 62]. By further increasing the temperature, water undergoes phase transitions into crystalline phases of water, composed of highly ordered arrangements of water molecules in tetrahedrally coordinated networks. The reported temperature for an irreversible phase transition to metastable cubic crystalline ice, I_c , varies widely between 120 and 160 K [63]. Increasing the temperature to ~ 200 K leads to a second phase transition into the stable crystalline form that predominates on Earth, hexagonal ice, I_h [55]. The phase transitions are accompanied by a reduction in vapour pressure [64] that allows the transformation to become visible in thermal and isothermal desorption experiments [38, 51, 59, 63].

3.4 Water-Graphite Interactions

Water adsorbs molecularly on graphite with a coverage-independent sticking coefficient of unity at low surface temperatures. Vibrational spectroscopy methods and density functional theory calculations reveal that water is physisorbed on graphite [40, 43, 44, 65–67]. At temperatures ≤ 100 K, ASW grows on graphite in a cluster growth mechanism [40, 43, 50, 51]. At low water exposures, water adsorption proceeds by nucleation at defect sites and subsequent formation of 2D clusters on the surface. When the exposure is increased, the growth proceeds with the formation of 3D islands owing to the low binding energy of water to graphite and the strong tendency of water to form the more stable intermolecular hydrogen bonds. At further increase of the exposure, larger hydrogen-bond networks of water multilayers are formed.

The presence of water clusters on graphite at low coverages becomes visible in temperature programmed desorption (TPD) studies [40, 43, 44, 50] (see Section 5.3 for more detailed information on the technique). At high coverages, water desorption exhibits a single peak in TPD spectra with a desorption energy of 0.41–0.45 eV/molecule, representing the desorption of water multilayers, *i.e.* water desorbing from water, or water sublimation. The determined desorption energy is very close to the sublimation energy of ice at 0 K of 0.49 eV/molecule, confirming the weak interaction of water with the graphite surface [56]. At low coverages, a peak at lower temperatures compared to the multilayer peak is present [40]. Both the phase transitions of ASW to cubic crystalline and the cubic crystalline to hexagonal crystalline ice can be observed through small shoulders on the low- and high temperature side of the TPD peaks, respectively.

3.4.1 Graphite Intercalation

The characteristic stacked structure of graphite and its electronic properties (see Section 3.1) make it possible to host a wide range of different atoms and molecules in the space between the graphene sheets [68]. The process is called *intercalation* and can be achieved by a charge transfer reaction. The intercalating species, called *intercalants*, are commonly divided into electron donor and electron acceptor compounds. The most common donor intercalants are alkali metals. As acceptor intercalants, many different reagents can be used, such as metal chlorides, bromides, fluorides and oxyhalides, acidic oxides and strong Brönsted acids such as H_2SO_4 and HNO_3 . The preparation of intercalated graphite compounds can start from solid, liquid or gaseous reagents. Molecular intercalants usually remain in molecular form upon intercalation. The intercalation process is energetically activated, as it is typical for diffusion phenomena, and it is driven by the charge-transfer between the graphene layers and intercalant species.

Evidence for water intercalation into the graphite sheets upon adsorption on graphite have been observed experimentally through additional TPD peaks of very low intensity at temperatures around 180 K [43]. Recently, energy barriers for intercalation of water into graphite have been obtained using density functional theory (DFT) calculations [67]. The energetic barrier for intercalation of a water ice bilayer was found to be low and the largest obtained barriers were in the order of a few hundred meV. However, the adsorption of water is energetically favoured compared to intercalation because the adsorption energy was found to be about half as high as the barrier for intercalation.

Zeolite Catalysts

Owing to their particular structural and chemical properties, zeolites are industrially utilised in a number of different ways. Examples of zeolite applications are molecular sieving for separation processes [69–71], water softening in detergents [72], and as catalysts for numerous chemical reactions [70, 73–75]. In the past 30 years, metal-exchanged zeolites have come into focus as catalysts for SCR of NO_x [29] replacing the first generation of catalysts commercialised for NO_x removal applications that consist of oxide-supported vanadia [76]. The development of zeolitic SCR catalysts started with the consideration of Cu- and Fe-ZSM-5 zeolites [77, 78], continued with the study of Cu- and Fe-beta zeolites [79, 80] until Cu-containing chabazite (Cu-CHA) zeolite materials were found and patented in the late-2000s. To date, these are the most stable and active catalysts for NH_3 -SCR [81–86]. Since 2010, they have been commercialised in diesel-vehicle aftertreatment systems as described in Section 1.2.

In this Chapter, the most relevant properties of zeolites for these studies and their synthesis will be described first, with a focus on chabazite. Then, different procedures for metal-ion exchange in zeolites will be discussed for the preparation of Cu-CHA. The last part of this section focuses on the state-of-the-art understanding of the mechanistic details of NH_3 -SCR over Cu-CHA catalysts.

4.1 Properties and Synthesis of Zeolites

Zeolites are microporous crystalline aluminosilicates, which can be either found naturally or synthesised. In 1756, the first zeolite was discovered by the

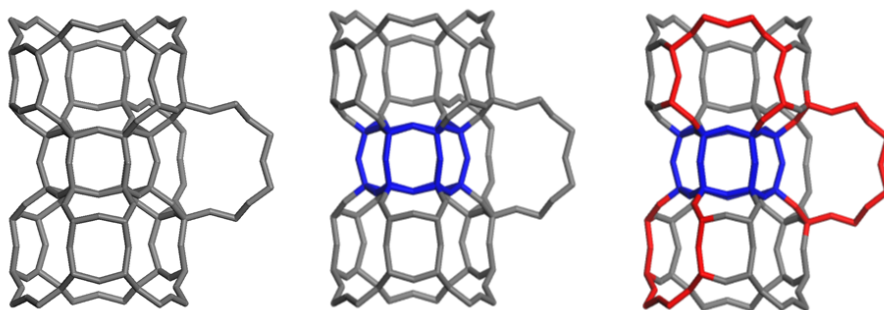


Figure 4.1: *Chabazite framework structure consisting of double six-membered rings (marked in blue) as building blocks interconnected by four-membered and eight-membered rings (marked in red).*

Swedish mineralogist Cronstedt, who named the new class of minerals derived from the greek words *zeo* and *lithos* meaning “boiling stone” [70].

In most zeolites, the primary structural units are SiO_4 and AlO_4 tetrahedra, interconnected by a shared oxygen atom [70]. They are arranged in simple polyhedrons, which act as the secondary building blocks, forming the final three-dimensional zeolite framework. As a result, the framework structure contains pores and intracrystalline channels. Each AlO_4 tetrahedron bears a negative charge that is compensated by an extra-framework cation occupying the voids. When at air and ambient conditions, water molecules are also present in the pores. Zeolites are classified according to their pore sizes, which can range between 0.3 and 1 nm. Small-pore zeolites typically exhibit a pore-diameter of 0.3–0.45 nm built by an eight-membered ring, as for example chabazite (CHA). Larger voids are created by medium-pore zeolites (10-ring pores with diameters of 0.45–0.6 nm) such as ZSM-5, large-pore zeolites (12-ring pores of 0.6–0.8 nm), e.g. zeolite Y, and extra-large pore zeolites (14-ring pores with diameters > 0.8 nm), such as UTD-1. Note that there is no systematic nomenclature for zeolite materials and that the acronyms are a more or less arbitrary invention of their discoverers.

The structure of a CHA zeolite is shown in Fig. 4.1. It consists of layers of double six-membered rings interconnected by four-membered and eight-membered rings resulting in a three-dimensional pore-system with a pore size of about 3.8 Å [70]. One of the synthetic zeolites with chabazite structure is called SSZ-13.

The Si/Al composition is another important characteristic of zeolites because it defines their acidity, thermal stability, hydrophobicity, and ion exchange capacity. The latter is determined by the number of Al atoms in the framework,

because of the introduction of an extra negative charge by every Al atom.

Zeolites can be synthesised by a hydrothermal approach which refers to a material formation in aqueous solution at elevated temperature. Silica is usually added in form of an alkali silicate, and the alumina source is typically an aluminium oxide or salt [70, 75]. Tetraalkylammonium cations, small amines, or other organic molecules are often used as structure-directing agents (SDA) in the synthesis, allowing the desired pores or channels to form around the hydrophobic organic species of matching size and geometry. The pH is an important factor in the synthesis and is usually carefully adjusted by hydroxide solutions. All components are combined in a certain order under agitation to form a gel before being transferred to an autoclave and left at temperatures around 50–300°C for several days while possibly being stirred [70].

4.2 Metal Ion-Exchange in Zeolites

For zeolite catalysts, it is often essential to introduce a transition metal ion into the pores in order to reach a high catalytic performance. This can be done by replacing the charge-compensating cation (often sodium after the synthesis) with the desired transition metal ion. Photographs of chabazite samples ion-exchanged with copper and iron are displayed in Figure 4.2. The most common way to prepare a copper-exchanged SSZ-13 zeolite, Cu-SSZ-13, is via an aqueous ion-exchange (AIE) route [87, 88]. For this purpose, the sodium form of the zeolite is first transformed into the hydrogen form (H-form) because protons can be more easily replaced by metal ions than sodium cations. This is done by a wet ion-exchange step with e.g. ammonium nitrate followed by a calcination of the material. Then, the H-form of the zeolite is suspended in an aqueous solution of a copper salt and stirred for typically several hours at elevated temperature and carefully adjusted pH. Sometimes the procedure has to be repeated in order to reach the desired ion-exchange level, also referred to as the Cu/Al ratio. Theoretically, if the introduced species is a Cu^{2+} cation, as proposed for aqueous ion-exchanged Cu-CHA (see Section 4.3), the maximum Cu/Al ratio should be 0.5 because two Al atoms are needed to compensate the charge of the divalent cation. This would then correspond to an ion-exchange level of 100%. In reality, it seems that the maximum loading can be higher than this, as outlined in Section 4.3.

Instead of using the conventional AIE method in the studies of this thesis, solid-state ion-exchange (SSIE) procedures were employed for the preparation of Cu-SSZ-13. A SSIE relies on bringing two solids to reaction at elevated temperature, and it exhibits several advantages compared to an AIE. In a SSIE procedure, several steps necessary in the AIE are bypassed, such as washing, filtering and drying of the product [89]. Thereby, the production



Figure 4.2: *Chabazite samples after ion-exchange with copper (left) and iron (right).*

of environmentally harmful copper-containing waste solutions is avoided. A SSIE route can be favourable for the introduction of transition metal ions which form large aqueous complexes, such as iron, especially when small-pore zeolites are used. In this thesis, two different SSIE approaches were applied, one was performed at high, and the other at low temperatures. In both cases, first physical mixtures of the zeolite (preferably in H-form) and the Cu salt or oxide are prepared by grinding or milling the powders. For the high temperature approach, the physical mixtures are transferred to an oven and stepwise thermally treated at air and a maximum temperature of ca. 800°C (see Paper II). This ion-exchange procedure is referred to as SSIE in this thesis. The high temperature allows a migration of Cu^{2+} ions into the zeolite pores along with the release of water. For the low temperature approach, NH_3 and NO gases are used during the ion-exchange to facilitate the introduction of metal ions [90] (see Paper III). This method is denoted as $[\text{NH}_3+\text{NO}]$ -SSIE. In this way, the ion-exchange temperature can be lowered to 250°C. As for the mechanism of the ion-exchange, Shwan *et al.* suggest that the Cu^{2+} species in the metal salt or oxide are first reduced by NO to form Cu^+ followed by the formation of $[\text{Cu}^+(\text{NH}_3)_x]^+$ ($x \geq 2$) complexes that can transport the Cu ions into the zeolite pores [90].

4.3 NH_3 -SCR Mechanism over Cu-CHA

Because of their excellent performance in NH_3 -SCR, the physicochemical properties of Cu-CHA have been studied intensely in the past decade with a wide variety of techniques in both the absence (*ex situ*) and presence of the reaction gases (*in situ* or *in operando*). This has led to an increasing understanding of the NH_3 -SCR mechanism over Cu-CHA zeolites. The main questions regarding the active catalytic sites can be summarised as follows: What are the active sites in the catalyst, where are they located, and what happens to

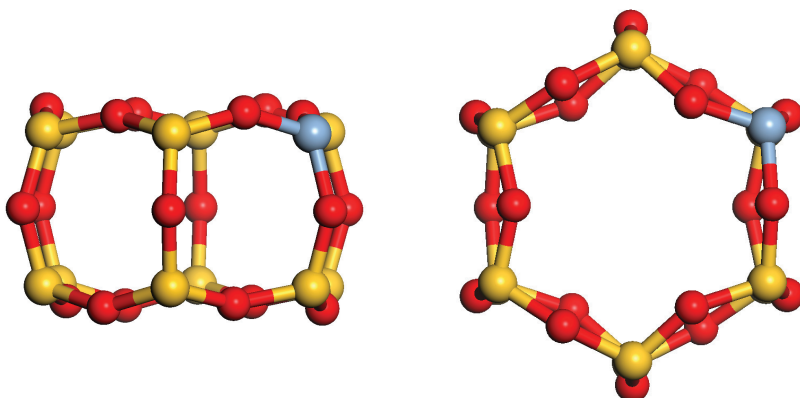


Figure 4.3: Double six-membered ring unit in chabazite in side view (left panel) and top view (right panel). Silicon atoms are marked in yellow, oxygen in red and aluminium in grey.

them during reaction conditions? Regarding the NH_3 -SCR over Cu-CHA it is still unclear what reaction intermediates are formed, and what the elementary and rate-determining steps of the reaction are. More specifically, how is NO activated in the reaction and what role do the Brønsted acid sites of the CHA framework play? In this section, the state-of-the-art knowledge of these questions will be outlined.

Ex situ studies mainly suggest that all Cu species in Cu-CHA are present as monomeric Cu^{2+} ions, and not as dimers or Cu_xO_y oligomers [87, 88, 91, 92]. Contradicting these observations, the presence of dicopper species in O_2 activated Cu-CHA, possibly originating from Cu_xO_y , has been proposed based on UV-Vis spectroscopy investigations [93]. Also using X-ray absorption near edge structure (XANES), indications of the presence of Cu oxides were found at high ion exchange levels [94]. Two distinct positions have been observed for Cu^{2+} in the CHA structure. The ions were both found to occupy positions in the double six-membered rings (6mr) (depicted in Figure 4.3) [87, 88, 92], as well as in the larger eight-membered ring (8mr) (depicted in Figure 4.4) at higher Cu concentrations [95, 96]. More specifically, in the 6mr, Cu^{2+} ions were found to occupy the faces of the rings [87], most likely slightly distorted from the center of the 6mr [88, 92]. By using a density functional theory (DFT) approach, Göttl *et al.* could distinguish more than the two different experimentally found positions for a Cu^{2+} ion in CHA as they took into account the distribution of the charge-compensating Al-atoms [97, 98]. For example, they showed that the Cu site located in the 6mr could give rise to two distinct peaks in diffuse reflectance infrared Fourier transform (DRIFT) spectra upon CO adsorption depending on whether one or two Al-atoms were

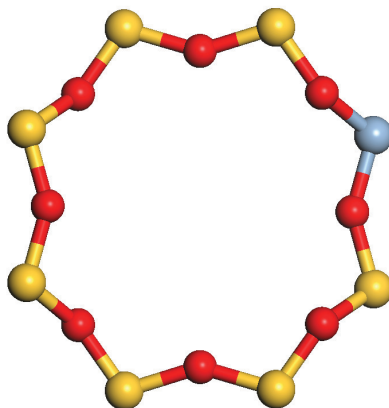


Figure 4.4: *Eight-membered ring unit in chabazite in top view. Silicon atoms are marked in yellow, oxygen in red and aluminium in grey.*

present in a 6mr.

In air and ambient conditions, water molecules are coordinated to the Cu^{2+} centres forming octahedral $[\text{Cu}(\text{H}_2\text{O})_6]^{2+}$ complexes as observed with UV-Vis spectroscopy, electron paramagnetic resonance (EPR), XANES and DRIFTS [92, 93, 99, 100]. When dehydrated by calcination or O_2 activation, a stronger interaction of the Cu ions with the Cu-CHA framework has been observed by formation of covalent Cu-O bonds with framework oxygen atoms [93]. More specifically, with XANES, Extended X-ray absorption fine structure (EXAFS) and XRD measurements, the formation of $[\text{Cu}^{2+}(\text{OH})]^{+}$ species in the 8mr has been observed, with the Cu having two framework oxygen linkages and one OH ligand [100, 101]. Indications of the formation of an OH-complex were also found with FT-IR investigations [93, 102, 103]. Interestingly, for the formation of a $[\text{Cu}^{2+}(\text{OH})]^{+}$ complex, charge compensation by two Al atoms in proximity is not required, so that Cu/Al ratios > 0.5 can be obtained (c.f. Section 4.2). Under SCR conditions and with increasing operation temperature, the Cu ions seem to migrate into the 6mr, and the maximum NO conversion seems to coincide with a positioning of the Cu ions in the 6mr as observed with in situ XRD [92]. Based on the findings of these studies, one important conclusion regarding the state and the position of the Cu species is that they are highly mobile and that their exact positions are determined by the ion exchange level and their interactions with the molecules in their environment. Therefore, a characterisation in ex situ conditions will give a different picture than in situ studies, when e.g. H_2O , NH_3 , NO_x or CO adsorbates will influence the position and the state of the Cu species [29].

Furthermore, under *standard* NH₃-SCR, the oxidation state of the Cu species in the zeolite was observed to change, i.e. both Cu²⁺ and Cu⁺ ions were found to coexist [104–106]. This implies that a redox reaction is part of the mechanism. The reducibility of a Cu²⁺ ion seems to be increased when being pulled out from its most stable position in the 6mr into the 8mr [95, 96, 107]. Interestingly, different kinetic regimes of the NH₃-SCR reaction have been observed [108], suggesting different mechanisms at different temperatures and Cu loadings. At high temperatures (> 350°C) and low Cu loadings, isolated Cu ions located in the 6mr are probably the active centers for the reaction. At low temperature (< 250°C), the Cu ions are observed to be mobile and solvated, while they experience a basic environment from stored H₂O and NH₃. A difference was observed within this temperature range between very low Cu loadings (Cu/Al < 0.044) where dimeric Cu-ions seem to dominate as active centers, and intermediate Cu loadings (0.044 ≤ Cu/Al ≤ 0.29) where monomeric Cu ions appear to be the active centers. An abnormal kinetic behaviour was observed between 250 and 350°C in which the Cu sites lose their extra-framework ligands and migrate to their most stable sites, the faces of the 6mr. This suggests that the monomeric sites at low and high temperatures exhibit different chemical environments [108].

Recently, two studies were published which suggest possible reaction mechanisms for *standard* NH₃-SCR (Equation 1.1) over Cu-CHA [105, 109] which seem to be different from that over V₂O₅-based catalysts. Both proposed mechanisms are similar, and consist of a reduction and an oxidation part, although different intermediates are proposed. Starting from a naked Cu²⁺ ion (Paolucci *et al.* [105]) or a Cu²⁺–OH[−] species (Janssens *et al.* [109]), NH₃ and NO are adsorbed under reduction of Cu²⁺ forming a Cu⁺H₂NNO (nitrosamide) complex. Release of a water and an N₂ molecule leaves a Cu⁺ ion behind that is oxidised in the next step. Janssens *et al.* then propose adsorption of first an NO and an O₂ molecule forming a nitrate complex (that has been observed spectroscopically [110, 111]) followed by adsorption of a second NO molecule and release of NO₂ forming a Cu²⁺NO₂[−] species for the case of standard NH₃-SCR. They highlight that the reaction mechanism of the fast NH₃-SCR reaction (Equation 1.2) is integrated in this cycle as adsorption of NO₂ on the Cu⁺ leads to formation of the same Cu²⁺NO₂[−] complex. Paolucci *et al.* suggest a similar oxidation step by NO and O₂ leading to a Cu²⁺NO₂ species but they take into consideration the involvement of a neighbouring Brønsted acid site that forms an NH₄⁺ species simultaneously. In contrast, Janssens *et al.* consider subsequent adsorption of NH₃ on the Cu site. The last step in both mechanisms is the release of another molecule of N₂ and H₂O leaving behind the Cu²⁺–OH[−] or Cu²⁺ ion the cycle started with, respectively.

In contrast to the proposed mechanism, the formation of an NO⁺ intermediate has been suggested during the Cu²⁺ reduction [96, 107, 110, 111]. Beale *et al.* argue that an involvement of adsorbed NO₂ and NH₄⁺ seems unlikely. Instead

they propose the formation of HNO_2 from $\text{Cu}^+ - \text{NO}^+$ with water. Indeed, the involvement of Brønsted acid sites in the cycle has been debated. On one hand it was found that the presence of H^+ seems beneficial as it leads to higher SCR rates [29]. On the other hand, NH_4^+ formed on Brønsted acid sites is less reactive than NH_3 bound to Lewis acid sites. Therefore, many researchers have proposed that the Brønsted acid sites can act as NH_3 storage in proximity to the active Cu sites [102, 103]. In particular, they can also attract more weakly bound NH_3 species on the NH_4^+ sites.

Despite the increasing knowledge about the mechanistic details of NH_3 -SCR over Cu-CHA zeolites, the full catalytic cycle at all operating temperatures and different Cu loadings is not known. An enhanced fundamental understanding of the mechanism is important as it may give an answer to the origin of the limited low-temperature activity of the Cu zeolites and lead to the development of even better performing NO_x reduction catalysts.

Characterisation Techniques

In this Chapter, the various characterisation techniques used in this work will be presented. Two different home-built experimental setups are used, an ultra-high vacuum chamber and a flow reactor system, which are introduced in the first section. Then, the basics of electron and atomic force microscopy are outlined. Temperature programmed desorption is described thereafter. Finally, a range of spectroscopic methods using light sources of different energies, *i.e.* infrared, visible and ultraviolet light, as well as X-rays, are presented.

5.1 Experimental Setups

The astrochemical studies were performed in an ultra-high vacuum chamber to approximate the low pressure in the interstellar medium (Paper I). For the NH_3 -SCR studies, different flow reactor systems were used for measurements of the catalytic activity of the copper zeolites and for temperature programmed desorption experiments using NO and NH_3 as probe molecules (Paper II and Paper III).

5.1.1 Ultra-High Vacuum System

The UHV system is composed of a cylindrical stainless steel chamber and described in detail in Ref. [112, 113]. The UHV chamber is pumped with a turbomolecular pump in combination with a cryogenic pump backed up by a mechanical pump to obtain an operational pressure of $\leq 5 \times 10^{-10}$ torr. Two

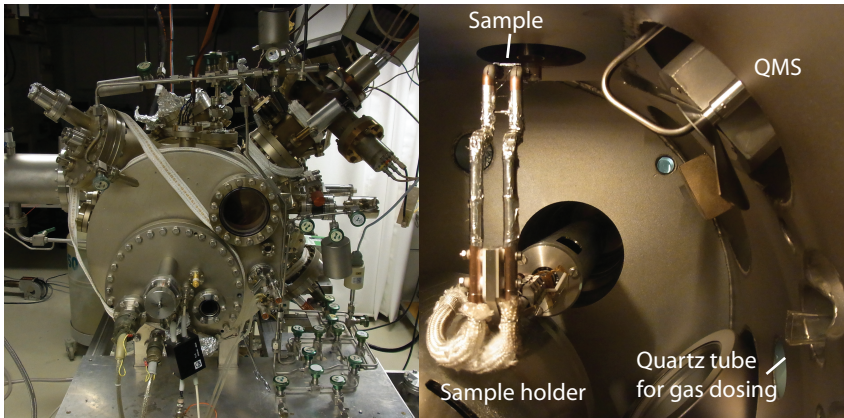


Figure 5.1: Images of the UHV chamber. Left panel: Outside view; right panel: View inside the UHV chamber showing the sample holder with attached sample on top, the quartz glass tube for gas dosing and the QMS.

vertical planes of the chamber are equipped with preparation and analytical equipment: different gas dosing units, thermal evaporation sources for metal deposition, a low-energy electron diffraction (LEED) analyser, an Auger electron spectrometer (AES), an electron-energy-loss spectrometer (EELS), and two quadrupole mass spectrometers (QMS, Balzers 311 and 511). The gas dosing unit for water deposition consists of a stainless steel gas reservoir and a gas line to the UHV chamber that is connected with a quartz-glass tube of a diameter of 8 mm inside the chamber. The pressure of the reservoir and gas line can be monitored by a capacitance manometer. A LabVIEW program (National Instruments) is used to acquire data from the gas exposures and the mass spectrometers. Irradiation, illumination of the sample, and detection of the reflected light from the sample is possible through UV-transmitting windows attached to the chamber.

The sample is mounted between two tantalum foil pockets that are connected to a sample manipulator, which allows movement in x, y and z-direction. The manipulator axis is parallel to the cylindrical axis of the chamber. The sample can be attached at the end of the manipulator in the radial direction. By moving the manipulator in the z-direction, the sample can be moved between the two planes, while rotation of the manipulator axis moves the sample in a circle to different positions for accessing different devices. Heating of the sample with defined temperature ramps up to 800 K is achieved by passing a current through it. The sample is cooled to ≤ 100 K by circulating liquid nitrogen through the copper rods of the manipulator. The temperature can be measured by a thermocouple that has been spot-welded to the tantalum sample holder.

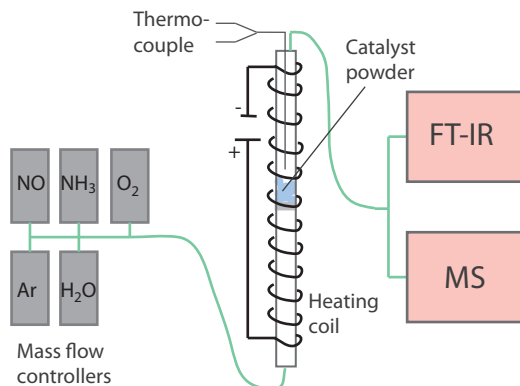


Figure 5.2: Schematic of a flow reactor system used in the NO_x reduction studies. The copper zeolite catalysts are present as powders in the vertical quartz glass tube. The gas flow of the reactant or adsorption gases is regulated by mass flow controllers. The catalyst can be heated electrically using either a heating coil or a furnace (not shown) and the temperature is controlled via a thermocouple that is placed in the gas stream at short distance from the catalyst powder. The effluent gases are continuously recorded by an FT-IR and/or mass spectrometer.

5.1.2 Flow Reactor System

A typical setup used for measuring the catalytic activity for NO_x reduction and performing temperature programmed desorption experiments using copper zeolites is schematically displayed in Figure 5.2.

The system consists of a set of Bronkhorst Hi-Tech LOW- Δ P-FLOW mass flow controllers (MFC) to regulate the gas flow of the reactant or adsorption gases, a quartz tube with the catalyst, and an MKS 2030 FTIR spectrometer and/or a Hiden HPR-20 mass spectrometer (MS). Gas flows between 20 and 300 ml/min with Argon as balance are used, depending on the particular system. The catalyst is placed in the quartz tube in powder form. For high gas flows, the powders are pressed to tablets and then crushed in order to obtain a larger particle size between 630 μm and 1.0 mm. The catalyst temperature is adjusted by electrical heating through either a heating coil or a furnace, and is controlled by a thermocouple that is placed in the gas stream at short distance from the catalyst powder.

5.2 Microscopy

The topography of the nanostructured graphite surface is analysed by atomic force microscopy (AFM) and scanning electron microscopy (SEM) (Paper I).

The zeolite samples are imaged by means of SEM and scanning transmission electron microscopy (STEM) (Paper II and Paper III). Localised chemical analysis of the samples imaged by SEM and STEM is performed with energy-dispersive X-ray spectroscopy (EDX).

Electron microscopy

Electron microscopes utilise an electron beam that is produced by heating a tungsten filament and focused by magnetic fields in high vacuum [114]. Owing to the short wavelengths of the electrons, resolutions down to 0.1 nm can be reached [114]. In scanning electron microscopy, accelerated electrons with energies of 0.1–30 keV from a finely focused beam are rastered across the sample surface [115]. Within an interaction volume, which is dependent on the acceleration voltage and can be up to several micrometers in dimension, the electrons interact with the specimen through elastic and inelastic scattering. Elastic scattering results in backscattered electrons which can be used to obtain images with compositional contrast. Inelastic scattering creates secondary electrons, which are usually used to obtain topographic information about the specimen. An SEM image is generated by conversion of the detected scattering signal intensity into a greyscale image. In this work, an LEO Ultra 55 SEM instrument was used.

For scanning transmission electron microscopy, a transmission microscope (TEM, FEI Titan 80-300TM) is used with a smaller probe of 10–15 nm which scans across the surface [114]. In TEM, a thin sample (up to about 200 nm) is subjected to an electron beam with an acceleration voltage of 60–300 keV. Instead of using the secondary or backscattered electrons as in SEM, the transmitted electrons are used in STEM. Either the direct or the diffracted beam can be detected creating a bright field or a dark field image, respectively [116].

Chemical analysis with Energy-dispersive X-ray spectroscopy (EDX) can be performed during SEM and STEM measurements using the X-radiation that the electron beam creates upon interaction with the specimen [116]. An X-ray detector that is mounted above the sample, can detect characteristic lines for each element from the emitted X-rays in addition to a continuous background spectrum caused by Bremsstrahlung.

Atomic Force Microscopy

With AFM, the height and diameter of the truncated cone structures of the nanostructured graphite surface can be obtained by mechanically probing the

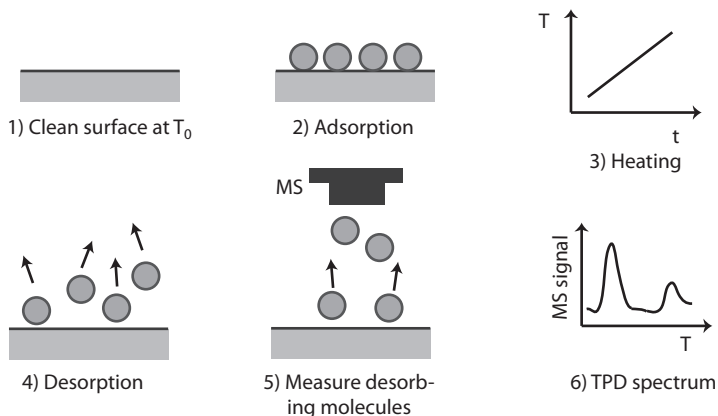


Figure 5.3: *Concept of the TPD method. The process starts by deposition of molecules onto a surface kept at a certain temperature (T_0) (1,2). A linear heating rate is applied (3) so that the molecules desorb (4) and the desorption rate is measured by e.g. a mass spectrometer (5). The resulting TPD spectrum (6) is a plot of the MS signal versus the temperature.*

surface with a sharp tip [117]. By scanning the surface laterally, the spatially varying forces between the oscillating tip and the surface can be converted into height information. Here, a DI-dimension 3000 SPM instrument was used.

5.3 Temperature Programmed Desorption (TPD)

The surface science technique TPD can be used to obtain energetic and kinetic information about interactions between adsorbates and the surface as well as between adsorbates [2]. In this thesis, TPD is used for both the astrochemical studies in a UHV system (Paper I) as well as for the studies of selective NO_x reduction in a flow reactor system at ambient pressure (Paper II). The concept of TPD is rather straightforward and illustrated in Figure 5.3. The procedure starts by exposing a surface that is cooled to a gas in order to adsorb molecules on the surface. The surface is heated by applying a (mostly) linear heating rate and the desorbing molecules are detected by a MS. By plotting the MS signal, that is proportional to the desorption rate, versus the sample temperature, a TPD spectrum can be obtained.

Adsorption

The gas adsorption procedures differ between the astrochemical and the emission control studies owing to the different experimental conditions, and are described as follows.

For adsorption of water to form ice on a nanostructured graphite surface, the sample surface is heated to 800 K in order to clean it from most adsorbates. Ultrapure water, kept in the gas reservoir, is degassed by repeated freeze-thaw cycles before the gas line to the chamber is evacuated and replaced by new water vapour. The surface can be exposed to water by two different dosing techniques: direct or background dosing. For direct dosing, the sample surface is positioned in front of the quartz-tube at a distance of ca. 1 mm. Exposing the surface to gas by direct dosing has the advantage that the rest of the chamber is not exposed to gas. However, it results in a more non-uniform coverage on the sample than for background dosing. For background dosing, the sample surface is at a position far away from the quartz-glass tube and the chamber is backfilled with the vapour. In the present studies, the cold (100 K) sample surface is exposed to water to a predetermined pressure for a measured length of time. Water exposures are expressed in langmuir (L), defined as 10^{-6} Torr s, corresponding to 4.79×10^{14} H₂O molecules cm⁻² s⁻¹ for a sticking coefficient of unity. Exposures obtained by direct dosing are calibrated by background dosing through comparison of the resulting TPD peak areas.

For adsorption of NO or NH₃ on copper zeolites, the samples are first heated to a temperature of 500 °C (773 K) in an Ar atmosphere with 8% O₂. The temperature is then kept constant at 150 °C (423 K) and the zeolite samples are exposed to 500 ppm of the adsorbate gas for three to four hours. After the adsorption step is completed, the system is flushed with Argon in order to remove any gas not adsorbed on the zeolite surface.

Thermal Desorption

After the exposure to gas molecules, thermal desorption of the adsorbates is induced by heating the sample with a linear heating rate β , *i.e.*

$$T_S(t) = T_0 + \beta \times t \quad (5.1)$$

where T_S is the sample temperature, t is time, and T_0 is the temperature at $t = 0$. Typical values of β are between 0.2–2.5 K/s. An MS is used to detect the desorbing products as a function of time. The MS can detect the

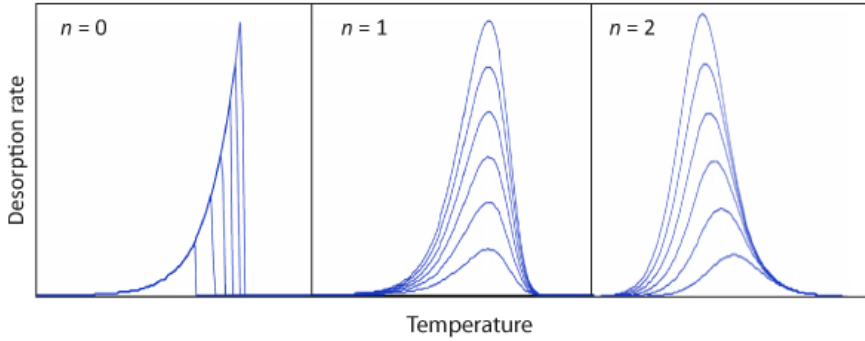


Figure 5.4: *Examples of TPD spectra of different desorption orders n and coverages.*

partial pressure increase caused by the desorbing species and discriminate it from species with different masses. The pressure change is proportional to the desorption rate of the adsorbate from the surface.

Hence, the desorption peak that is observed in TPD spectra results from changes in the desorption rate. It contains information about kinetic parameters of the desorption process that will be explained in the following Section.

Analysis of TPD spectra

Despite the simplicity of the TPD concept, the obtained TPD spectra are rich in information. Examples of computed TPD spectra are shown in Figure 5.4. Both energetic and kinetic parameters can be obtained from TPD spectra [2]. The desorption rate that has been given in Equation 2.2 can be expressed including the pre-exponential factor A , the coverage Θ , and the desorption order n in the proportionality constant:

$$r_{\text{des}} = -\frac{\partial\Theta}{\partial t} = A\Theta^n \exp\left(-\frac{E_{\text{des}}}{RT}\right) \quad (5.2)$$

where E_{des} is the activation energy for the desorption process, T the temperature, and R is the gas constant with $R = k_{\text{B}} \times N_{\text{A}}$ where N_{A} is the Avogadro constant. This equation is called Polanyi-Wigner equation.

If the sample is heated in a linear fashion, Equation 5.2 becomes:

$$-\frac{\partial\Theta}{\partial T} = \frac{A\Theta^n}{\beta} \exp\left(-\frac{E_{\text{des}}}{RT}\right) \quad (5.3)$$

The desorption order n can take values of $n = 0, 1, 2$. Zero-order desorption is often observed for multilayer coverages, *e.g.* H₂O/HOPG. Examples of first-order desorption ($n = 1$) are atomic or simple molecular desorption, *e.g.* CO/Cu. Second order desorption ($n = 2$) will usually be present for recombinative molecular desorption, *e.g.* O₂/Pt or H₂/Ni.

For a zero-order desorption behaviour ($n = 0$), Equation 5.2 can be simplified to:

$$r_{\text{des}} = A \exp\left(-\frac{E_{\text{des}}}{RT}\right) \quad (5.4)$$

In this case, the desorption energy is independent of the coverage of the adsorbates. Examples of TPD spectra of a zero-order desorption process are shown in Figure 5.4. The desorption temperature (peak maximum) increases with increasing coverage. The slope of the high-temperature side of the zero-order desorption peaks is determined by how fast the molecules are removed from the MS detector, *i.e.* the pumping speed of the pumps in the vacuum chamber. Ideally, the slope is infinitely high. Rewriting of Equation 5.4 leads to:

$$\ln(r_{\text{des}}) = \ln(A) - \frac{E_{\text{des}}}{R} \frac{1}{T} \quad (5.5)$$

An Arrhenius analysis yields the desorption energy and pre-exponential factor by plotting $\ln(r_{\text{des}})$ as a function of $\frac{1}{T}$. This results in a straight line with a slope of $-\frac{E_{\text{des}}}{R}$ and a y -axis intercept of $\ln(A)$.

For a first-order process ($n = 1$), the desorption rate is proportional to the coverage if A and E_{des} are independent of the coverage. A molecular, non-associative desorption from a surface is usually of first order. TPD spectra for a first-order desorption process are also presented in Figure 5.4. It becomes clear that the desorption temperature is constant and independent of the coverage.

In a second-order desorption process ($n = 2$), the desorption rate is proportional to the coverage squared. Second-order desorption kinetics can be observed in the case of associative desorption resulting in TPD spectra that share a common trailing edge at different coverages, as shown in Figure 5.4. The desorption temperature decreases with increasing coverage. Also for systems of first order desorption behaviour with coverage-dependent desorption energies, desorption curves with these characteristics can be observed. This is the case for inhomogeneous substrates that exhibit a large variety of adsorption sites of different energies.

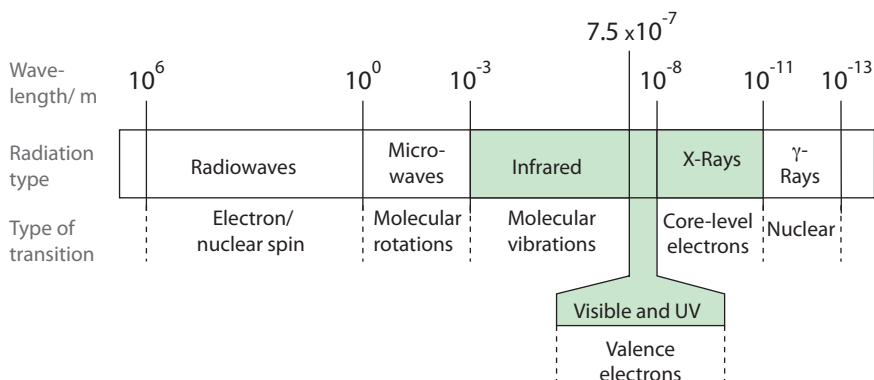


Figure 5.5: *The electromagnetic spectrum. Radiation types marked in green are those that are used in the present work.*

TPD spectra can contain several peaks of different desorption orders which may overlap. The features in the TPD spectra, *e.g.* the number of peaks or shoulders, give information about the number of inequivalent adsorption sites that are occupied. The whole integrated peak area corresponds to the initial adsorbate coverage. If an absolute initial coverage is known through other measurements, *e.g.* LEED measurements in UHV, the absolute coverage at each temperature can be determined. However, if multiple inequivalent adsorption sites are present that result in multiple TPD peaks, the calculated coverage under each peak does not necessarily correspond to the initial coverage at each adsorption site, because diffusion between the different adsorption sites can take place during the temperature increase.

5.4 Spectroscopy

In spectroscopic measurements, the interaction of light (electromagnetic radiation) with matter is utilised to gain valuable information about material properties. Light of different energies (wavelengths) can induce different transitions in a molecule, see Figure 5.5.

In this thesis, spectroscopic techniques which involve infrared (IR), visible (vis), ultraviolet (UV), and X-radiation are used. The light can be absorbed, emitted, transmitted or scattered (reflected) by the material. Here, light scattering (reflection) is utilised in several different spectroscopic techniques and systems and is described in more detail in the following paragraph before the basics of each spectroscopic technique used is outlined.

Light scattering means that the incoming light is deflected at the surface. One

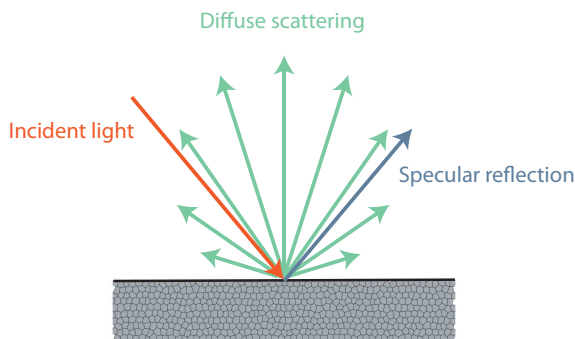


Figure 5.6: Schematic of the specular reflection (blue arrow) and diffuse light scattering (green arrows) phenomena.

can distinguish between specular and diffuse reflection (or scattering), shown in Figure 5.6. If light is specularly reflected, the incident light ray is reflected at the surface like a mirror. This is described by the law of reflection which states that the angle of incidence (with respect to the surface normal) equals the angle of reflection. Diffuse reflection is due to scattering that occurs in the surface. Parts of the incident light rays are scattered at the boundaries of the crystallites that build up the surface. It results in a randomised direction of the outgoing light. The intensity of the diffusely reflected light can be approximated by Lambert’s cosine law, which states that the intensity of the scattered light in an angle Θ with respect to the incident light follows a $\cos(\Theta)$ distribution. This means that the larger Θ , the lower the intensity of the scattered light.

5.4.1 UV-vis Spectroscopy

Shining light at UV and visible wavelengths on liquid and solid substances can excite transitions from their occupied orbitals into non-occupied orbitals. In the case of copper zeolites, transitions in the d-band of *e.g.* Cu^{2+} ions ($3d^9$) can be observed [93]. If coordinated to water or zeolite framework atoms, the five d orbitals can split, thus allowing for electronic transitions within the d-band. For Cu-CHA, this results in a spectral feature observed at 730–1100 nm [118]. Electronic transitions are also possible between the central ion and its ligands, they are referred to as ligand-to-metal charge transfer (LMCT) transitions. For copper zeolites, a transition $\text{O}^{2-}\text{Cu}^{2+} \longrightarrow \text{O}^-\text{Cu}^+$ can occur between 230–360 nm for Cu-CHA samples [118].

In this work, UV-vis spectroscopy in diffuse reflection is used for probing the

copper species present in the zeolite samples (Paper II and Paper III). Furthermore, the desorption of water molecules from a nanostructured graphite surface is analysed by UV-Vis spectroscopic measurements in diffuse reflection. The experimental details of both techniques are described in the following paragraphs.

Optical Sample Characterisation in a Spectrophotometer

To optically characterise the zeolite samples, a spectrophotometer was used. The samples are used as powders in sufficient thickness to be non-transmitting, so that

$$A \approx 1 - S \quad (5.6)$$

where A is the fraction of the light being absorbed, and S the fraction of light being scattered (reflected) from the sample.

Hence, the absorption can easily be calculated by measuring the light being scattered (reflected) by the sample. The measurement was performed using a Varian Cary 5000 spectrophotometer with an integrating sphere (Internal DRA 2500). A sketch of a typical setup for an absorption measurement of non-transmitting samples with an integrating sphere detector is shown in Figure 5.7. The sample is irradiated with monochromatic light through a hole in the sphere (red arrow in Figure 5.7). The specularly (blue arrow) and diffusely reflected light (green arrows) from the sample surface hits the integrating sphere which is coated with a highly reflective material, polytetrafluoroethylene (PTFE). The coating is able to diffusely reflect 99% of all light between wavelengths of 350 and 1800 nm. Thus, almost all (specularly and diffusely) reflected light from the sample can reach the detector that is located at the bottom of the sphere.

Optical Detection during Water Desorption from Nanostructured Graphite

In order to follow the thermal desorption of water from the nanostructured samples optically, the thermal desorption experiment with MS detection described in Section 5.3 was modified. In particular, the intensity of the diffusely reflected light from the sample in specular direction was measured simultaneously to the recording of the MS signal. This was made possible by two windows that were attached to the UHV chamber at an angle of 60° . A scheme

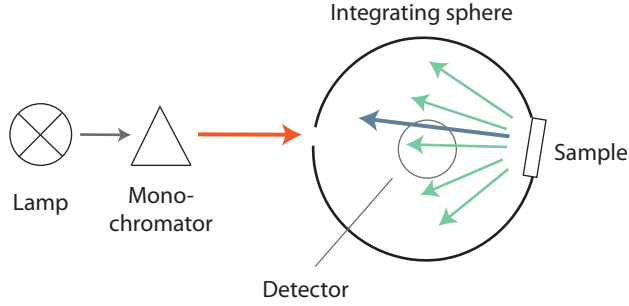


Figure 5.7: Setup of a typical absorption measurement of non-transmitting samples: Monochromatic light (red arrow) hits the sample and the specularly (blue arrow) and diffusely scattered light (green arrows) is detected using an integrating sphere.

and pictures of the experimental setup for the optical detection technique are shown in Figure 5.8.

The water ice-covered surfaces were illuminated with UV and visible light through one of the UV transmittant window on the vacuum chamber. Two different light sources were used: an arc lamp (100 W Hg, mounted inside a housing with elliptical reflectors from Photon Technology Inc., positioned behind a water filter that removes IR-radiation) and a UV light emitting diode (LED; Hamamatsu LC-L2, calibrated $\lambda=365$ nm).

The scattered light was detected with a CCD detector (AvaSpec-3648 with grating UA for $\lambda=172\text{--}1100$ nm) through an optical fiber (Avantes, diameter: $400\mu\text{m}$) fixed at the other window. The fiber was connected to a collecting lens in order to increase the detected light intensity. Optical spectra were recorded with the software AvaSoft (version 7.5) during a temperature ramp of 0.5 K/s between 100 and 400 K. With a QMS that was close to the sample, TPD spectra could be recorded simultaneously.

For data analysis, the light intensities of the reflected light at 365 nm were extracted and plotted against the temperature T . The resulting curves $R(T < 300\text{ K})$ were normalised to the blank intensity $R_{\text{blank}}(T)$ at temperatures $T > 300\text{ K}$, when all water was desorbed. Hence, the reflected light intensity R is defined as follows:

$$R = \frac{R(T < 300\text{ K})}{R_{\text{blank}}(T > 300\text{ K})} [\%] \quad (5.7)$$

A quantity ΔR was defined as difference in R between the blank (at $T = 300\text{ K}$) and the ice covered surface (at $T = 100\text{ K}$), *i.e.*:

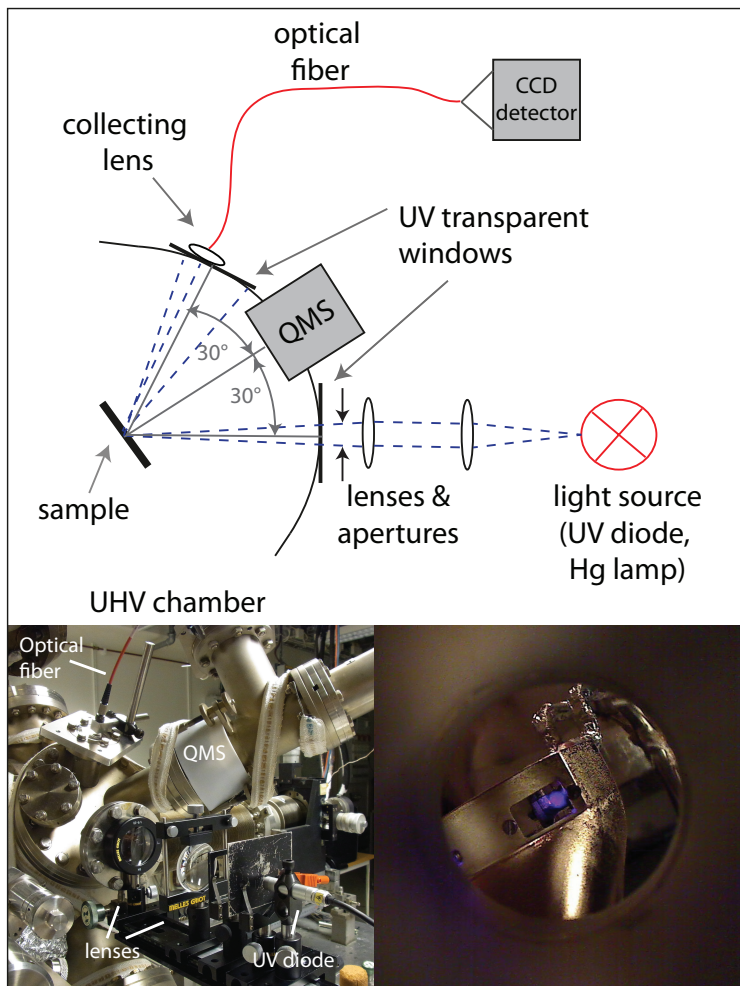


Figure 5.8: The experimental setup to measure TPD spectra with combined detection by QMS and by tracking the diffusely reflected light from the surface in specular direction. Top: A scheme of the setup. Bottom: A picture of the setup from the outside (left panel) and a view on the sample through the detecting window (right panel).

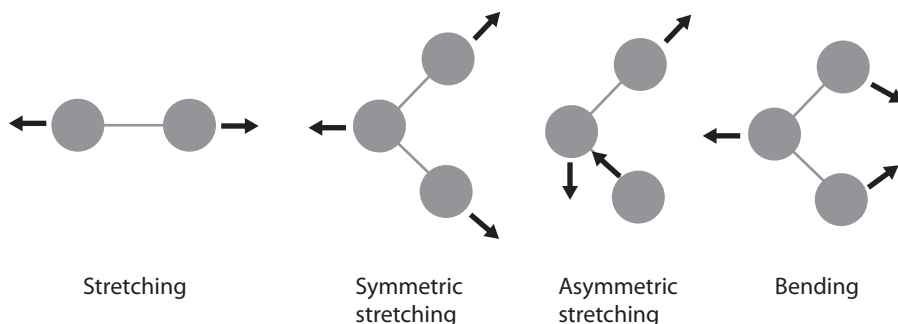


Figure 5.9: *Some typical vibrations of two- and three-atomic molecules.*

$$\Delta R = R(300 \text{ K}) - R(100 \text{ K}) \quad (5.8)$$

For further data analysis, the first derivative of R , $\frac{dR}{dT}$, was taken. Derivative methods were introduced in the 1950s and are commonly used in analytical spectroscopy because they exhibit some advantages for the analysis of optical spectra [119]. In general, the enhanced complexity of derivative spectra can be useful for characterising materials and to distinguish two substances from each other. Furthermore, derivation enables a background elimination as well as a discrimination of overlapping optical bands. Here, the first derivative represents the rate of change of the optical signal with the temperature, and the peak areas correspond to the slope of the increase of the optical signal.

5.4.2 Infrared Spectroscopy

Transitions between the vibrational levels of a molecule can occur upon absorption of infrared photons [120]. The number of fundamental vibrations is $3N-6$ for non-linear and $3N-5$ for linear molecules with N atoms, and four different types of vibrations can be distinguished, stretching, bending in plane and out of plane, and torsion vibrations. Some examples of fundamental vibrations of two and three-atomic molecules are shown in Figure 5.9. The vibrations can only be clearly observed if the dipole moment changes during the vibrations. Therefore, *e.g.* molecular N_2 is dipole forbidden and absorbs infrared light only weakly, whereas CO , NO and OH exhibit strong infrared bands.

In this work, IR spectroscopy is employed using a Fourier Transform infrared spectrometer to analyse the reaction products in catalytic activity measurements (Paper II and Paper III), as well as using diffuse reflectance infrared Fourier transform spectroscopy (DRIFTS) in order to gain information about

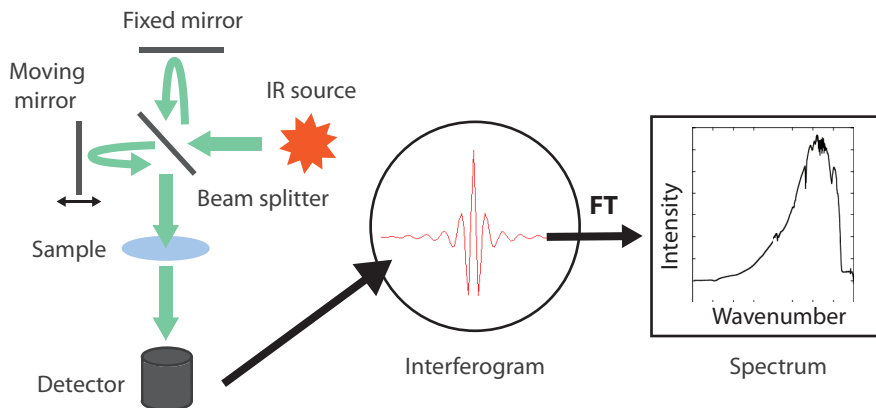


Figure 5.10: *Schematic setup of an FT-IR spectrometer.*

the chemical state and location of the copper species in the zeolite samples (Paper IV).

Transmission Fourier Transform Infrared Spectroscopy

A Fourier Transform infrared (FT-IR) spectrometer uses a so-called Michelson interferometer instead of prisms or grids as in traditional spectrometers [121]. The main advantages are that all wavenumbers can be analysed simultaneously and that the signal-to-noise ratio is enhanced when using an interferometer. A schematic setup of an FT-IR spectrometer is displayed in Figure 5.10. Light from an IR source hits a beam splitter that reflects one part of the light that is directed to a fixed mirror. The other part of the light is transmitted by the beam splitter and reflects in a moving mirror. The recombined beams are sent through the sample to the detector. Because one mirror is mobile, the intensity of the light collected on the detector is dependent on the position of the mirror. The resulting interferogram shows the intensity as a function of the path difference which is represented by a quadratic cosine function if monochromatic light is used. For polychromatic light, the quadratic cosine functions interfere and give rise to an interferogram that is the sum of those functions. A spectrum (intensity versus energy) can be created with the raw data in the interferogram by applying a common algorithm, the Fourier transform. In the activity measurement of the copper zeolite materials, an MKS 2030 FTIR spectrometer is used for a quantitative analysis of the effluent gases, in particular ammonia and NO_x gases.

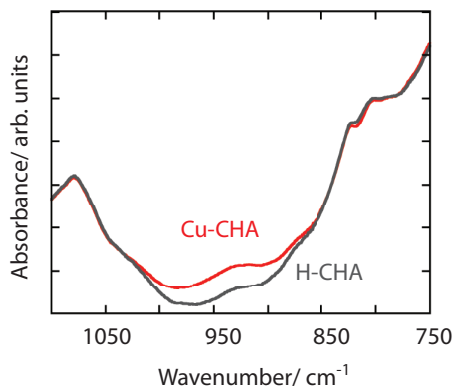


Figure 5.11: DRIFT spectra of the asymmetric T-O-T stretching vibrations of the zeolite framework with $T = \text{Si}, \text{Al}$ for the H-CHA and Cu-CHA materials.

Diffuse Reflectance Infrared Fourier Transform Spectroscopy

One tool used for the characterisation of the copper zeolite samples is DRIFTS. Here, a Biorad FTS6000 spectrometer with MCT detector and equipped with an in situ high-temperature reaction cell was used. The setup of a DRIFT spectrometer is similar to the transmission FT-IR instrument described above. The difference is that instead of measuring the transmitting light, the diffusely scattered radiation from the sample surface is collected with parabolic mirrors and reflected to the IR detector [121]. In addition, the powder sample is installed in a small reaction cell, allowing the introduction of probe molecules or reaction gases. The technique can be used in situ and time-resolved changes in the surface species can be recorded. This allows the investigation of the zeolite materials by probing the different copper species with appropriate probe molecules, such as CO or NO. However, DRIFT background spectra of the zeolites (before exposing the samples to probe molecules) can also provide useful information. For example, in Figure 5.11, DRIFT spectra of H-CHA and Cu-CHA zeolite materials that are used in this work are presented. The asymmetric T-O-T stretching vibrations of the zeolite framework ($T = \text{Si}, \text{Al}$) in the region between 860 and 1030 cm^{-1} are found to be more pronounced for the Cu-CHA than for the H-CHA material. Hence, with these DRIFTS measurements, the successful introduction of Cu species in the zeolite framework can be confirmed.

5.4.3 X-ray Diffraction

X-ray diffraction (XRD) is used to investigate the crystal structure of the zeolite samples after the solid-state ion-exchange as well as to identify the different phases present in the samples. A Siemens D5000 diffractometer was used in addition to the I711 beamline of Max II (MAX IV Laboratory, Lund, Sweden) giving high-resolution X-ray diffractograms. Diffraction at the crystal planes of solids can take place if the wavelength of the incident light is in the same order of magnitude as the interlayer spacing of the crystals [114]. Because the spacing between the arrays of atoms or ions in crystalline solids is in the order of 100 pm, commonly X-rays from K_α of Cu (154.18 pm) are used. Reflection occurs only if the conditions for constructive interference are fulfilled which are described by the Bragg equation [114]:

$$n \lambda = 2 d_{hkl} \sin \Theta_{hkl} \quad (5.9)$$

where λ is the wavelength of the incoming X-rays, d_{hkl} is the spacing between the crystal planes with Miller indices hkl , and Θ_{hkl} is the Bragg angle, *i.e.* the angle of incidence between the X-rays and the crystal planes. Powder samples consist of a large number of crystallites that are oriented randomly with respect to one another. The diffraction of X-rays will only occur from those planes that are oriented in the correct angle to fulfill the Bragg condition. Because the planes can lie in all directions, the crystallites produces reflections that are located on the surface of cones with a *semi*-apex angle of 2Θ . During a measurement, the sample is usually rotated to maximise the number of planes in the diffraction condition. From the resulting powder diffraction patterns, the d_{hkl} spacing for each reflection can be assigned. High-resolution X-ray diffraction (HR-XRD) patterns can be obtained using synchrotron radiation that are at least five orders of magnitude more intense [114].

For high-symmetry crystal systems, as zeolites, the Rietveld method can be used to solve the crystal structure from diffraction patterns [114]. Both the line positions and intensities are interpreted by assigning each peak a gaussian shape so that an overall line profile can be calculated. Usually, one starts with a trial structure that is then gradually modified by changing the atomic positions until the best fit is obtained.

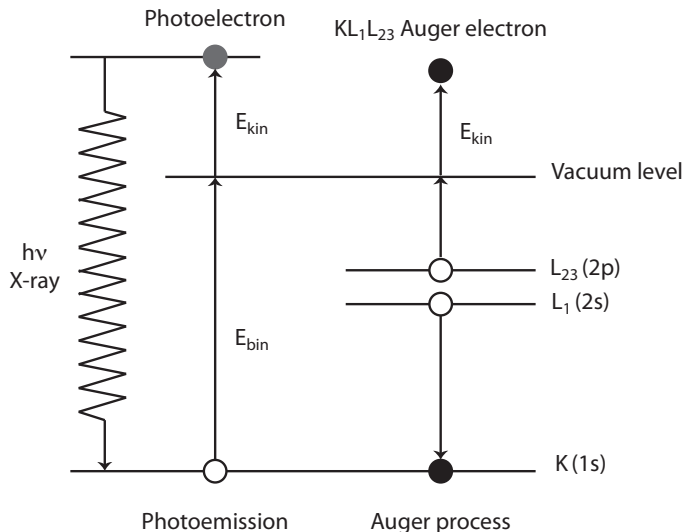


Figure 5.12: Principle of the photoemission and the Auger process that are the basis for XPS and AES, respectively.

5.4.4 X-ray Photoelectron and Auger Electron Spectroscopy

X-ray photoelectron spectroscopy (XPS) and Auger electron spectroscopy (AES) are used in this work to study the copper species in the prepared Cu-CHA samples. The XPS and AES investigations were performed with a PerkinElmer PHI 5000C ESCA system. Both techniques can be used to gain surface-sensitive information about the elemental composition of the sample and its chemical state [120]. XPS is based on the photoelectric effect which implies that an atom absorbs an incoming photon, leading to the ejection of a core or valence electron. The resulting photoelectron has a kinetic energy E_{kin} that is dependent on the incoming energy of the photon, $h\nu$ and the binding energy, E_{bin} [122], *i.e.*:

$$E_{kin} = h\nu - E_{bin} \quad (5.10)$$

The photoemission process is illustrated in Figure 5.12. By measuring the intensities of the emitted photoelectrons as a function of their kinetic energy, the binding energy of an electron can be derived. Binding energies are characteristic for an element and its oxidation state. Apart from the emission of a photoelectron, the Auger process can take place during an XPS measurement which is also shown in Figure 5.12. The ejected electron (*e.g.* from a K shell)

leaves a hole that can be filled by a less energetic electron (*e.g.* from a L_1 shell). The remaining energy is transferred to another electron (*e.g.* in a L_{23} shell) that can be emitted with a certain kinetic energy. In contrast to the photoemission process, the kinetic energy of an Auger electron is independent of the energy of the incoming photon energy but characteristic for the element and oxidation state.

If the photoelectron transfers energy to another electron of the atom, shake-up or shake-off losses can arise [122]. Shake-up lines can be observed if this electron is in a higher unoccupied state, whereas shake-off lines are observed if the electron is in an unbound state. Because the photoelectron has lost part of its kinetic energy, the shake-up and shake-off lines will appear at higher binding energy in the XP spectrum. Discrete shake-up lines are prominently observed for some transition metal oxides, such as nickel, iron, cobalt, and copper. They can give useful additional information because the losses depend on the environment of the atom.

Results and Discussion

In this Chapter, the results are summarised and discussed. First, the characterisation of the properties of the studied materials, nanostructured graphite (NGS) and Cu-CHA, are outlined, before the investigations of the interaction between the surfaces and adsorbates from both TPD and spectroscopy studies are presented. Finally, findings from activity measurements of the Cu-CHA samples for the NH_3 -SCR reaction are discussed.

6.1 Characterisation of Materials Properties

Various microscopic and spectroscopic methods have been used to characterise the nanostructured and microporous surfaces.

Imaging of the samples by microscopic methods is valuable in order to reveal the different species and dimensions of the features present on the surfaces. In case of the NGS, scanning electron and atomic force microscopy are employed and reveal the presence of well defined graphite nanostructures in the shape of truncated cones that cover approximately 30% of the rough surface, see Figure 6.1 (Paper I). The upper and lower diameter of the structures can be estimated to about 190 nm and 100 nm, respectively, and the height is measured to about 100 nm. The rough surface features exhibit a characteristic size of <50 nm.

In order to study the microporous copper chabazite samples, SEM is used (Paper II) along with STEM (Paper III). These electron microscopy investigations reveal the cubic shape of the chabazite crystallites, and enable to map the distribution of copper species outside and inside the zeolite crystallites, in

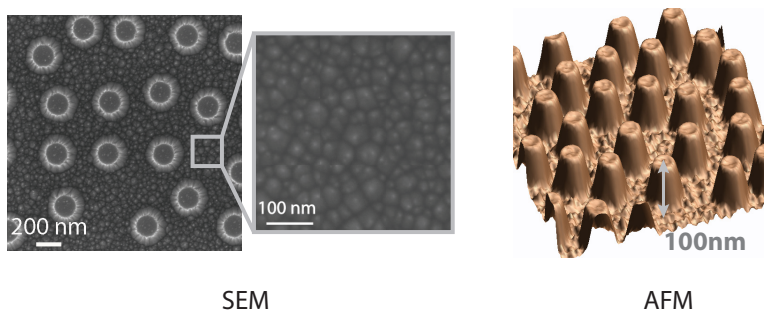


Figure 6.1: The NGS imaged by SEM (left panel) and AFM (right panel). The AFM image (size (xyz) : $2.5\ \mu\text{m} \times 2.5\ \mu\text{m} \times 100\ \text{nm}$) of the surface is visualised with the WSxM 3 software [123].

particular if used in combination with chemical analysis by EDX, as shown in Figure 6.2. In the physical mixture of CHA and CuO, before employing the $[\text{NH}_3+\text{NO}]$ -SSIE, copper oxide crystallites are visible outside the zeolite crystallites. After the $[\text{NH}_3+\text{NO}]$ -SSIE, the presence of Cu inside the zeolites can be detected, thus verifying the insertion of Cu species in the micropores of the zeolites.

The Cu-CHA samples prepared by SSIE and SSIE-SCR are further characterised by spectroscopic methods, such as X-ray diffraction, UV-Vis and X-ray photoelectron and Auger electron spectroscopy and some of the results are highlighted here (Paper II). The maintained crystallinity of the Cu-CHA samples after SSIE is confirmed using XRD. High resolution XRD further reveals the presence of CuO in both the SSIE and the SSIE-SCR samples, as well as the presence of Cu_2O in the SSIE-SCR sample, see Figure 6.3a.

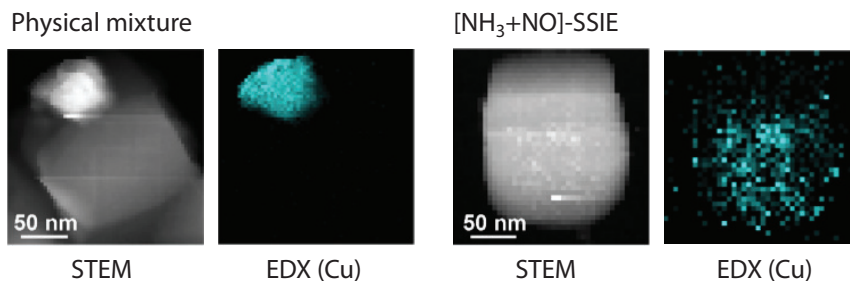


Figure 6.2: STEM images of a Cu-CHA sample showing the zeolite crystallites and the Cu distribution as analysed by EDX in the physical mixture of CHA and CuO and after the $[\text{NH}_3+\text{NO}]$ -SSIE.

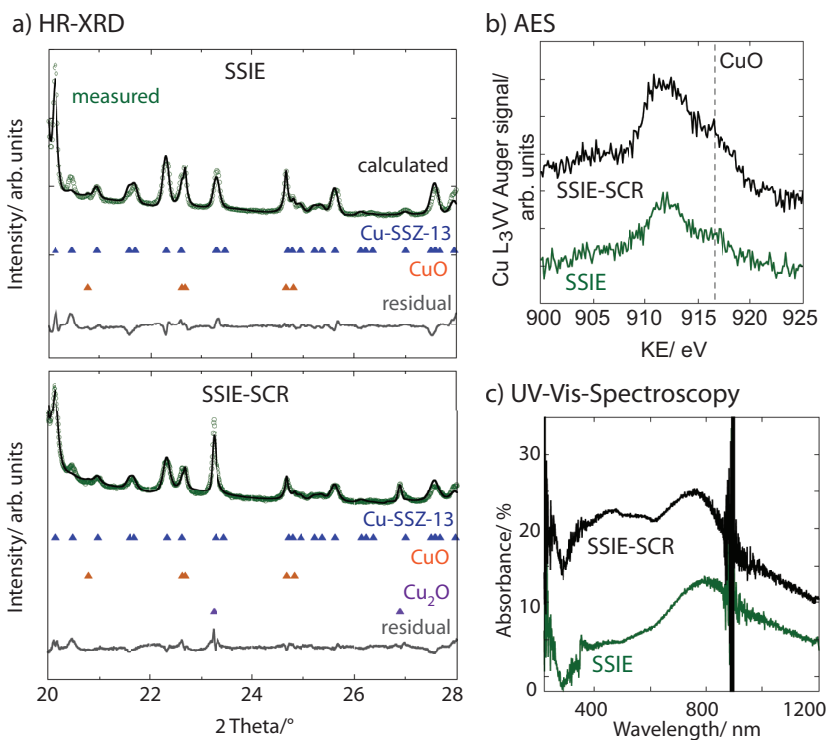


Figure 6.3: Characterisation of the SSIE and SSIE-SCR Cu-CHA samples by different spectroscopic methods. a) HR-XRD results of the samples with 2.0 wt% Cu (a), AES (b) and UV-Vis-spectroscopy results (c) of the samples with 2.7 wt% Cu

The Cu L₃VV Auger line observed in XPS experiments can be used to probe the oxidation state of the Cu species in the Cu-CHA samples, see Figure 6.3b. A significant shift of 5 eV to lower kinetic energies (KE) is observed compared to a CuO reference, which is indicative of an incorporation of the Cu in the zeolite pores after the solid-state ion-exchange. In addition, the increased width of the main Auger feature suggests the presence of species in two different oxidation states, e.g. Cu⁺ and Cu²⁺ cations.

UV-Vis spectroscopic measurements of the Cu-CHA samples suggest a high number of absorption peaks in the solid-state ion-exchanged samples studied in this thesis, see Figure 6.3c. Apart from the LMCT transitions at 230–360 nm and the d-d-transitions between 730–1100 nm that are commonly observed for aqueous ion-exchanged samples as reported in literature, also bands at 400–550 nm are present for the Cu-CHA samples prepared by SSIE. These features are observed to grow in intensity after exposing the samples to NH₃-SCR reaction conditions and can likely be associated with Cu⁺ species.

6.2 Interactions between Molecules and Surfaces

The study of the interaction between molecules and surfaces can serve two different purposes. One is that probe molecules can help to characterise the surface as they can interact distinctively with particular features of the surface. This is utilised in the DRIFTS studies of this thesis (Paper IV) where CO and NO are used as probe molecules to characterise the Cu(I) and Cu(II) species present in the Cu-CHA samples. It is also used in the TPD experiments using NH_3 which can bind to both the Brønsted (proton) and Lewis (Cu) acid sites, and using NO which binds to solely the Lewis acid sites in the Cu-CHA samples, respectively (Paper II). In addition, also the properties of the interaction itself can be of interest. This is the case for the DRIFTS studies with NO, as well as the TPD experiments with NH_3 and NO, because the probe molecules are also present as reactants in the NH_3 -SCR reaction. Furthermore, the interaction between water and the NGS is studied using TPD and a spectroscopic method in order to reveal the impact of the graphitic nanostructures on the kinetics and energetics of thermal water desorption (not published). In the following paragraphs, these findings are discussed divided into results from i) TPD and ii) spectroscopy experiments.

6.2.1 Temperature Programmed Desorption Results

The obtained TPD spectra of both water adsorbed on the NGS (Paper I) and NH_3 adsorbed on the Cu-CHA samples prepared by SSIE-SCR (Paper II) contain multiple overlapping peaks, see Figure 6.4. These peaks correspond to different binding sites on the samples, that in the case of the NGS are introduced by the nanostructured features of the surface, and in the case of the Cu-CHA samples are owing to the presence of various Cu species in the microporous structure of the zeolite. This gives also rise to kinetic effects that complicate the analysis of the spectra.

The H_2O -TPD peaks observed for the NGS (left panel in Figure 6.4) can be assigned to water desorption from 2D (peak A) and 3D (peak B) H-bonded ice, defect-bound water caused by oxygen plasma etching (peak C, D) and water intercalated into open graphite sheets of the truncated cone structures (peak E, F). Thus, compared to TPD spectra of water adsorbed on pristine graphite and rough (oxygen plasma etched) graphite, the NGS gives rise to additional features in TPD spectra.

The NH_3 -TPD spectra of copper chabazites (right panel in Figure 6.4) can be deconvoluted using three different gaussian peaks. Peak α and β have been observed to increase with increasing copper content which is indicative of a contribution of Cu sites to these peaks. For peak γ , no clear trend with

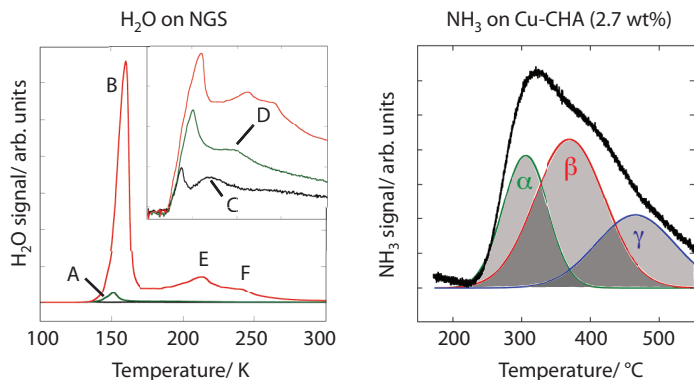


Figure 6.4: TPD spectra of molecules adsorbed on two different surfaces used in this work. Left panel: Water on nanostructured graphite at exposures of 0.3, 2.9 and 53 L, the inset shows the same spectra in logarithmic scale over the same temperature range; Right panel: NH_3 on Cu-CHA prepared by SSIE-SCR containing 2.7 wt%.

increasing copper content can be observed, which suggests that kinetic effects are likely present, such as diffusion limitations and readsorption issues owing to the microporous structure of the zeolite. Nevertheless, all three peaks probably result from Cu sites in the zeolite because no good fit could be obtained for a H-CHA sample using peaks at the same desorption temperatures as for Cu-CHA. In general, NH_3 is thought to affect the mobility of the Cu sites in the zeolite, an effect that is used for the low-temperature SSIE in a reactive NH_3 and NO atmosphere. Naturally, this further complicates the interpretation of the measured TPD spectra.

6.2.2 Spectroscopy Results

In addition to detecting the MS signal during a TPD experiment (Paper I), the intensity of light reflected from the ice-covered NGS can be measured during water desorption, see Figure 6.5. Compared to TPD with MS detection, where the desorbing species are measured, here, the remaining adsorbates and the state of the substrate are probed. The difference between the intensity of the reflected light from the ice-covered and the blank NGS is specified as ΔR . As displayed in Figure 6.5, ΔR is linearly dependent on the ice thickness. Water ice coverages as low as 0.4 nm (corresponding to about 3 L water exposure) can be detected by this method. Furthermore, a sudden decrease in the reflection signal is noted (as indicated by the arrows in the right panel in Figure 6.5). In TPD experiments reported in literature, a phase transition of water from ASW to cubic crystalline ice can be observed at the same temperature. The variation

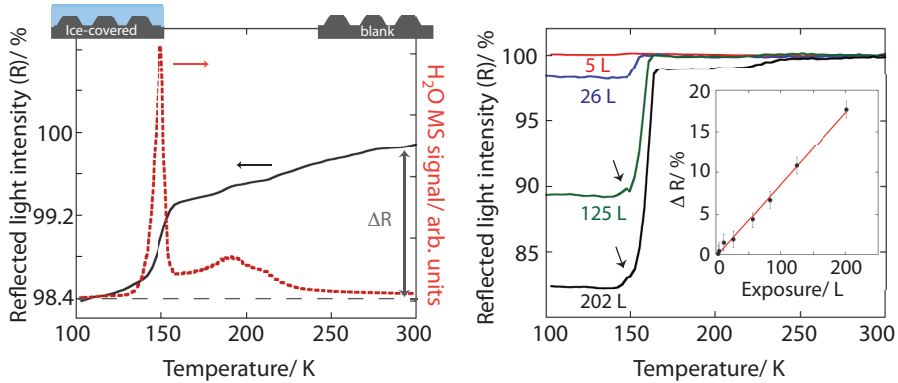


Figure 6.5: Left panel: Reflected light intensity (R) and the MS signal during thermal desorption of water from the ice-covered (12L) nanostructured graphite surface with a heating rate of 0.5 K/s. Right panel: Reflected light intensity (R) during TPD for different water exposures. The arrows mark the decrease in signal intensity owing to water crystallisation. The inset shows the linear dependence between difference ΔR and water exposure. Error bars are derived from the instrumental error in the instruments.

of the reflection signal can be understood by a change of the refractive index of the system during the crystallisation. The refractive index of ASW has been observed to increase linearly from 1.20-1.27 for temperatures between 20 and 120 K, to reach constant values of 1.285 ± 0.01 [124] and 1.31 [125] at temperatures above 140 K. The change in refractive index is directly related to the increase of ice density through the Lorentz-Lorenz relation [124, 125].

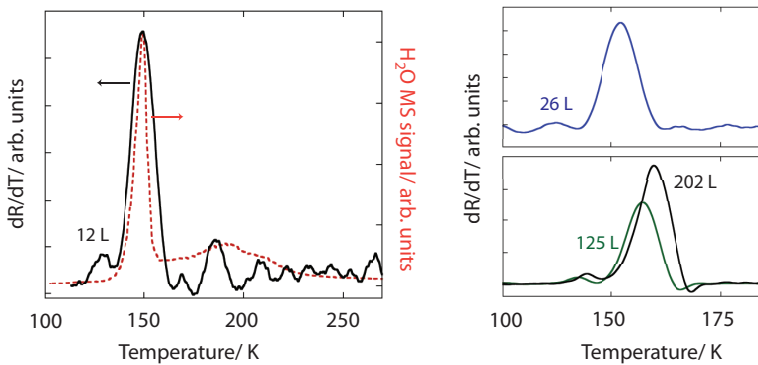


Figure 6.6: Left panel: First derivative of the reflected light intensity for a water exposure of 12L shown in the left panel of Fig. 6.5 shown together with the MS signal. Right panel: Derivatives for exposures of 26, 125 and 202 L.

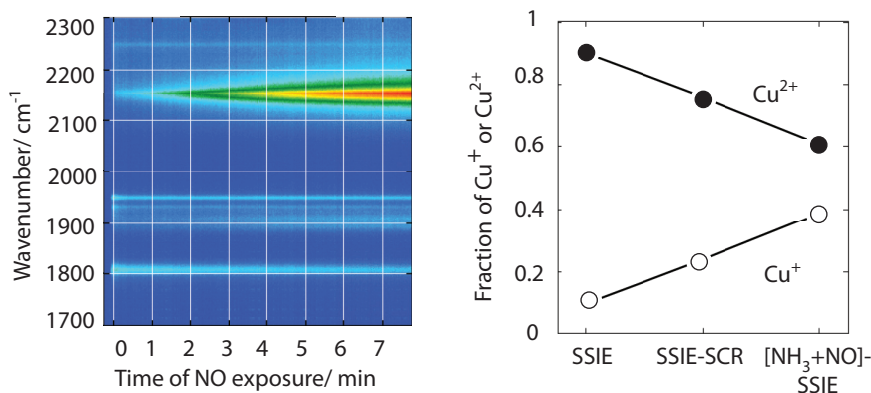


Figure 6.7: Left panel: *In situ* DRIFT spectra of the SSIE-SCR ion-exchanged Cu-CHA samples during exposure to NO at 20 °C. The red colour corresponds to the highest, and blue to the lowest intensities. Right panel: Estimated fraction of Cu²⁺ and Cu⁺ species present in the samples, as derived from analysing the NO-DRIFT spectra at 3 s of NO exposure.

By taking the first derivative of the reflection signal, the good agreement between the MS and the reflection signal for the peak at ca. 150 K corresponding to multilayer water desorption is apparent, as displayed in Fig. 6.6. Furthermore, taking the derivative of the signal is advantageous to better resolve the crystallisation peak which can be observed at 129–144 K for water exposures of 12–202 L.

Spectroscopy of adsorbed molecules on the sample surfaces is also utilised for characterisation of the Cu-CHA samples, *i.e.* in DRIFTS studies. With DRIFTS using CO and NO as probe molecules, further insights into the location and oxidation state of the Cu species in the micropores of the zeolite can be provided (Paper IV). In the left panel of Figure 6.7, *in situ* DRIFT spectra of the SSIE-SCR ion-exchanged Cu-CHA sample is shown during exposure to NO at 20 °C. NO can be used as a probe for both Cu²⁺ and Cu⁺ species. The peak that is centered at 2150 cm⁻¹ can be assigned to NO⁺ bound to Cu⁺ after autoreduction of Cu²⁺ species by NO [107]. The peaks in the range of 1890–1949 cm⁻¹ correspond to NO bound to Cu²⁺ species [107, 126, 127] and the peaks at around 1808 cm⁻¹ can be associated with NO bound to Cu⁺ species [107]. The relative peak intensities change with increasing NO exposure. Likely, this is owing to both kinetic effects during adsorption of NO and multiple chemical reactions that can take place upon NO adsorption on the Cu sites altering their oxidation state. Therefore, it is most feasible to perform an estimation of the fraction of the Cu⁺ and Cu²⁺ species present in the samples after a short time of NO exposure as displayed in the right panel of Figure 6.7.

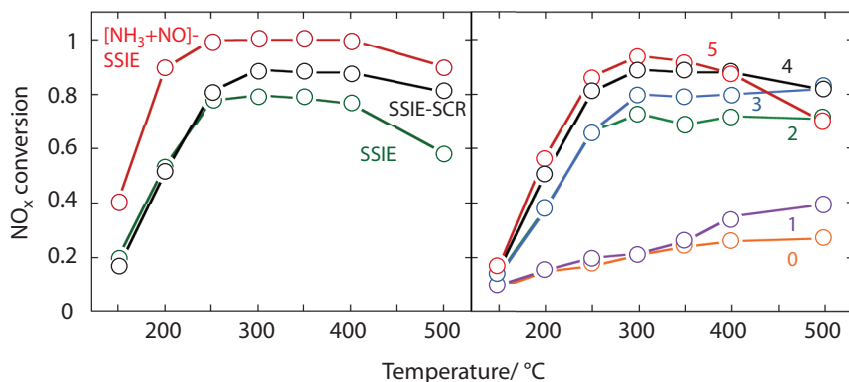


Figure 6.8: Catalytic activity of Cu-CHA samples for NH_3 -SCR. Left panel: Cu-CHA containing 4 wt% Cu prepared by different methods of solid-state ion-exchange; right panel: Cu-CHA prepared by SSIE-SCR with varying amounts of Cu (1–5 wt%) and H-CHA (0 wt%).

The fraction of Cu^+ species is observed to be highest (ca. 40%) in the sample prepared by $[\text{NH}_3+\text{NO}]$ -SSIE, followed by the sample prepared by SSIE-SCR. The SSIE sample exhibits the lowest fraction of Cu^+ species (ca. 10%).

6.3 Catalytic Surface Reactions

The catalytic activity of the solid-state ion-exchanged Cu-CHA samples for NH_3 -SCR is examined in this work in order to evaluate their applicability for NO_x abatement and to draw conclusions about the extent of catalytically active species introduced into the micropores of the zeolite. In Figure 6.8, the NO_x conversions of Cu-CHA samples prepared by different solid-state ion-exchange methods as well as of Cu-CHA with different Cu contents and H-CHA are shown. The activity curves displayed in the left panel of Figure 6.8 are obtained with Cu-CHA samples that contain 4 wt% Cu which corresponds to a Cu/Al ratio of 0.5 for the SSIE and SSIE-SCR sample and to a Cu/Al ratio of 0.6 for the $[\text{NH}_3+\text{NO}]$ -SSIE sample.

The catalytic activity for NH_3 -SCR is highest for the $[\text{NH}_3+\text{NO}]$ -SSIE sample at all temperatures, reaching full NO_x conversions at 250–400 °C. The sample prepared by SSIE-SCR shows the second highest activities for NH_3 -SCR with a maximum NO_x conversion of 90% at 300 °C. Compared to the SSIE-SCR sample, the NO_x conversion is reduced for the sample prepared by SSIE at temperatures between 300 and 500 °C.

With increasing Cu content, the NO_x conversion is generally observed to increase, as shown in the right panel of Figure 6.8 for Cu-CHA samples prepared by SSIE-SCR. However, there are three exceptions. The sample containing 1 wt% shows only a slight increase in NO_x conversion by max. 15% points at temperatures of 400–500 °C. The samples containing 2 and 3 wt% show the same NO_x conversions at temperatures between 150 and 250 °C. It can also be observed that the NO_x conversions of the sample with 5 wt% Cu drops below the value of the samples containing 3 and 4 wt%.

These activity measurements can together with the results of the characterisation of the Cu-CHA samples presented in Section 6.1 and 6.2 aid the understanding of the extent and kind of active species inserted into the micropores of the zeolite. As reviewed in Section 4.3, isolated Cu^{2+} ions are believed to act as catalytically active species in the NH_3 -SCR reaction over Cu-CHA. In the reaction mechanisms proposed in literature [105, 109], the autoreduction of the catalytically active species to Cu^+ is suggested to be crucial. Here, the $[\text{NH}_3+\text{NO}]$ -SSIE sample, which shows the lowest amount of Cu^{2+} and the highest amount of Cu^+ species, exhibits the highest activity in NH_3 -SCR. However, with the $[\text{NH}_3+\text{NO}]$ -SSIE preparation method the highest total number of Cu species are anticipated to migrate into the zeolite micropores. Furthermore, the presence of CuO in the samples is observed to be lowest for this sample and highest for the SSIE sample. This leads to the conclusion that the total number of Cu species present in the micropores of the chabazite is more important than the oxidation state of the species. Presumably, all species are oxidised to Cu^{2+} species under the reaction conditions (oxygen excess).

By inserting 1 wt% Cu in the zeolite pores, a Cu/Al level of 0.1 is obtained and only the most stable Cu sites are filled. The results shown in the right panel of Figure 6.8 suggest that these sites are not the most active ones because an increase in NO_x conversion compared to a H-CHA sample is only observed at temperatures between 400 and 500 °C. Insertion of 2 wt% Cu in chabazite (Cu/Al = 0.3) allows the most active sites for NH_3 -SCR to be occupied as the relative conversion increase with respect to the Cu content is highest between 1 and 2 wt% Cu. This site can presumably be filled up continuously when increasing the amount of Cu in the samples up to 5 wt% which is the highest amount investigated here. The third kind of Cu species that shows an increased activity at temperatures between 150 and 250 °C is inserted by increasing the Cu content from 3 wt% (Cu/Al = 0.4) to 4–5 wt% (Cu/Al = 0.5–0.7).

For all samples with a Cu content equal to or above 4 wt%, the NO_x conversions are observed to decrease at a temperature of 500 °C. This is likely owing to a direct oxidation of NH_3 by molecular oxygen bypassing the reduction of NO_x that is more favourable at high temperatures. Direct ammonia oxidation is also increased in the presence of copper oxides which is in line with both the most significant decrease in activity for the SSIE sample exhibiting the highest

fraction of copper oxides, and the enhanced decrease for samples containing high total amounts of Cu. This conclusion is strengthened by the observation of a maintained NH_3 conversion at $500\text{ }^\circ\text{C}$ (not shown).

The presence of Cu oxides, *i.e.* an incomplete ion-exchange, in the solid-state ion-exchanged Cu-CHA samples is probably also the reason why no saturation in conversion, can be observed for the SSIE-SCR samples despite being commonly measured for aqueous-ion-exchanged Cu-CHA. Nevertheless, for Cu-CHA samples prepared by $[\text{NH}_3+\text{NO}]$ -SSIE, a saturation in conversion could be observed at Cu contents from 3 wt% corresponding to a ratio $\text{Cu}/\text{Al}=0.5$ (not shown). This further confirms that the Cu ions are more efficiently introduced in the chabazite pores by an $[\text{NH}_3+\text{NO}]$ -SSIE as compared to an SSIE-SCR approach, where up to a Cu/Al ratio of 0.7, no saturation in NO_x conversion is observed.

Conclusions and Outlook

This thesis comprises studies of thermal water desorption from a nanostructured graphite surface and investigations about the nature of the copper species in solid-state ion-exchanged copper chabazite.

In contrast to the majority of previous thermal desorption studies in the area of astrochemical surface science, we have introduced a nanostructured surface as substrate. This surface can be considered as a more realistic model grain core than the standard model surfaces. The more complicated surface morphology of the nanostructured graphite surface has shown to strongly affect the kinetics and energetics of the desorption process. For example, desorption of defect-bound water was observed resulting in an enhanced desorption energy for water desorption relative to the desorption energies for water desorption from pristine graphite. Furthermore, signs of intercalation of water into the graphite sheets were found indicating a possible enhanced accessibility of the intersheet openings due to the nanostructuring. The commonly applied detection of the QMS signal of the desorbing species was complemented with a spectroscopic detection method using light reflection from the surface which allows for a characterisation of the remaining adsorbate. Using this method, water ice coverages as low as 0.4 nm could be observed in addition to the water phase transition from amorphous to crystalline water ice.

One can see many possibilities for future research on this topic. The HCL-based fabrication method of the nanostructured substrate enables the design of a broad spectrum of nanostructured surfaces for usage as dust grain models. It is possible to use other materials with compositions similar to interstellar dust grain cores, as for example glassy carbon, fused silica or a combination of both. Future studies could investigate the influence of the surface material, as well as

of the dimensions and shape of the nanometric features on the desorption processes of water or other molecules. One can also imagine further research on chemical reactions using nanostructured dust grain model surfaces motivated by the well-known catalysing effect of defect sites and nanostructures. One example may be an investigation of the hydrogen formation mechanism, which is still not fully understood although molecular hydrogen is the most abundant molecule in the interstellar medium. Because the employed nanostructuring of a graphite surface has also been observed to change the light absorption and reflection properties of the material, the optical detection technique may be further studied with other substrates of varying dimensions and at different wavelengths of the incoming light. With the aim to further enhance the sensitivity of the optical detection method, it might also be possible to make use of the sensing potential of plasmonic absorptions by using substrates that are fabricated with additional metal nanoparticles.

Within the area of selective NO_x reduction, the properties and catalytic activity for NH_3 -SCR of Cu-CHA prepared by different approaches of solid-state ion-exchange have been investigated. After the SSIE procedure at 800°C in air, CuO crystallites were found outside the zeolite crystallites. However, after exposure to NH_3 -SCR conditions, the CuO signatures were observed to decrease and an enhanced activity for NH_3 -SCR was found. Simultaneously, both the formation of external Cu_2O crystallites and an increase in Cu(I) and Cu(II) species inside the zeolite pores was found, likely originating from the CuO present after the SSIE. The concept of a reaction-driven ion-exchange was further applied for the preparation of Cu-CHA samples by an SSIE in a reactive NH_3/NO atmosphere at 250°C . Cu-CHA samples prepared by this $[\text{NH}_3+\text{NO}]$ -SSIE were found to exhibit complete NO_x conversions at temperatures between 250°C and 400°C . The use of a physical CuO/CHA mixture containing 2 wt% Cu was found to be the most favourable in the $[\text{NH}_3+\text{NO}]$ -SSIE in order to obtain high NO conversions and to avoid a decrease in activity at high temperatures. The location and oxidation state of the copper species in the zeolite micropores were found to vary between Cu-CHA samples prepared by SSIE, after subsequent exposure to NH_3 -SCR conditions and to samples prepared by $[\text{NH}_3+\text{NO}]$ -SSIE. In particular, the fraction of Cu(I) species was estimated to be highest for the $[\text{NH}_3+\text{NO}]$ -SSIE (40%) and lowest for the SSIE sample (10%). The locations of the Cu(I) species in the zeolite micropores, however, were not found to differ between the different samples whereas the locations of the Cu(II) species were found to be sensitive to the SSIE procedure.

As an outlook for the studies in this field, further investigations of the $[\text{NH}_3+\text{NO}]$ -SSIE seem promising thanks to the easier preparation method of Cu-CHA compared to an AIE approach and the excellent activities of the samples for NH_3 -SCR. The mechanism of the Cu insertion into the zeolite using $[\text{NH}_3+\text{NO}]$ -SSIE is worth clarifying, possibly leading to the discovery of other molecules

that can assist the Cu diffusion into the chabazite micropores. Furthermore, SSIE methods offer the possibility to insert metal ions into small-pore zeolites that only exist in bulky complexes in water, which limits the AIE procedure. Hence, the preparation of an iron-containing Fe-CHA or a bimetallic Fe/Cu-CHA material containing both Fe and Cu ions may be realised in future by using a solid-state ion-exchange approach. These materials can potentially exhibit higher NH_3 -SCR activities at low temperatures compared to Cu-CHA that only reaches full NO_x conversion from temperatures of 250°C . The lack of low-temperature activity may be owing to the adsorption of water blocking the active sites for the reaction. Future studies could focus on a way to remove that water or to create active sites that are less favourable for water adsorption.

Acknowledgements

During the course of this thesis work, I encountered many important persons who have helped me develop on both an academic and a personal level.

First of all, I would like to thank Hanna Härelind, Per-Anders Carlsson and Magnus Skoglundh for supervising me on the copper zeolite project. You have never complained about helping me in the lab, reading my articles and discussing results with me. Hanna, thank you for your support whenever I needed it and for providing me feedback on this thesis.

I also want to thank my examiner Henrik Grönbeck who has helped in many occasions. Thank you too for reading this thesis and providing feedback!

The emission control project has been performed within the Competence Center for Catalysis which is funded by the Swedish Energy Agency, Chalmers University of Technology and the member companies: AB Volvo, ECAPS AB, Haldor Topsøe A/S, Scania CV AB, Volvo Car Corporation AB and Wärtsilä Finland Oy. I got frequent help (even late at night and at weekends) from my colleagues in the lab, thank you so much, Alexander Shishkin, Emma Adams, Pooya Tabib Zadeh Adibi and Kirsten Leistner!

Dinko Chakarov, Henrik Grönbeck and Lars Hellberg are gratefully acknowledged for the supervision of the astrochemistry part of this thesis. Lars is especially acknowledged for all the technical and mental support in the lab.

The astrochemistry work was funded by the EU initial training network LASSIE

that was both educationally valuable and fun to be a part of. During these occasions, I've met amazing people some of which became close friends, thank you guys for the fun on our various trips!

In rough times, people have listened to me and helped me finding solutions. I'm very grateful for that, Julie Gold, Peter Apell and Lena Falk.

I want to thank all current and former members of the Chemical Physics and the Applied Surface Chemistry divisions for the pleasant atmosphere around the office, talking nonsense at fikas and playing sports with me. Some more people deserve mentioning because they have put up with discussing science with me frequently, they are (in no particular order): Igor Zoric, Fernando González-Posada, Carl Wadell, Kristina Wettergren, Anders Hellman, Adam Arvidsson, Pooya Tabib, Jenny Andersson, Alexander Shishkin and Maxime Van den Bossche (and probably many more). Thanks!

Gratitude also goes to my (quite numerous) office mates: Gustav, Natalia, Pooya, Ben, Maxime, Kristina, Jenny, Natalia and Rickard (in chronological order, I believe). You have all tolerated my occasional swearing at computers in german, and both my silent and chatty periods.

My current and previous housemates had to endure a lot, tack så jätte mycket, Ruggero and Belinda! Doris och Bengt är de snällaste hyresvärderna som finns, tusen tack för att ni har förgyllt min tid i Göteborg! There are more people who have made my life in Gothenburg fun, Tina, Joachim, Adriana, Brita, Gülis, Jenny, Ben, Francesco, Virginia, Valentina, Angelika, Lovisa, Carl, Pooya, Maxime, Mokhtar, Sheedeh, Emma, Freddy and Dave, tack and thank you!

Chris, you are wonderful and I am grateful for every second we have spent together, thanks for your support in tough and stressful times, for celebrating the achievements along the way with me, and for being so enthusiastic when it comes to science. In thesis-related matters, I thank you for frequently discussing scientific and linguistic topics with me and for giving me feedback on my articles and thesis.

I have truly amazing friends around the world who are not being scared off easily by the lack of proximity and contact: Steffi, Annika, Tina, Lina, Farah, Lena, Verena, Belinda and Ulli, you are great.

I can't imagine a better family than the one I have. Danke, Mama, Papa, Maike und Elisa, für eure Selbstlosigkeit, eure Unterstützung und euer immerwährendes Interesse fuer meine Arbeit. Und noch wichtiger: Ihr versteht die Wichtigkeit von Care-Paketen!

Bibliography

- [1] I. Chorkendorff and J. W. Niemantsverdriet. *Concepts of Modern Catalysis and Kinetics*. Wiley-VCH, 2007.
- [2] K. W. Kolasinski. *Surface Science*. John Wiley & Sons Ltd, 2002.
- [3] A. G. G. M. Tielens. *Physics and Chemistry of the Interstellar Medium*. Cambridge University Press, 2005.
- [4] <http://www.astro.uni-koeln.de/cdms/molecules>, The Cologne Database for Molecular Spectroscopy (CDMS), Universität zu Köln, 21/10/2015.
- [5] A. C. Cheung, D. M. Rank, C. H. Townes, D. D. Thornton, and W. J. Welch. Detection of Water in Interstellar Regions by its Microwave Radiation. *Nature*, 221:626–628, 1969.
- [6] R. J. Gould and E. E. Salpeter. The Interstellar Abundance of the Hydrogen Molecule. I. Basic Processes. *Astrophys. J., Suppl. Ser.*, 138:393–407, 1963.
- [7] D. Hollenbach and E. E. Salpeter. Surface Recombination of Hydrogen Molecules. *Astrophys. J.*, 163:155–164, 1971.
- [8] T. A. Pauls, T. L. Wilson, J. H. Bieging, and R. N. Martin. Clumping in Orion KL-2-arcsecond maps of ammonia. *Astron. Astrophys.*, 124:23–38, 1983.
- [9] K. M. Menten, C. M. Walmsey, C. Henkel, and T. L. Wilson. The centimeter transitions of E-type methanol. *Astron. Astrophys.*, 157:318–328, 1986.

- [10] S. B. Charnley, M. E. Kress, A. G. G. M. Tielens, and T. J. Millar. Interstellar Alcohols. *Astrophys. J.*, 448:232–239, 1995.
- [11] D. A. Williams and E. Herbst. It’s a dusty Universe: surface science in space. *Surf. Sci.*, 500:823–837, 2002.
- [12] Z. Tan, H. Chihara, C. Koike, H. Abe, K. Kaneko, K. Sato, and S. Ohara. Interstellar Analogs from Defective Carbon Nanostructures account for Interstellar Extinction. *Astron. J.*, 140:1456–1461, 2010.
- [13] W. W. Duley and A. Hu. The 217.5 nm band, infrared absorption, and infrared emission features in hydrogenated amorphous carbon nanoparticles. *Astrophys. J.*, 761:115, 2012.
- [14] Y. Carpentier, G. Féraud, E. Dartois, R. Brunetto, E. Charon, A.-T. Cao, L. d’Hendecourt, Ph. Bréchnignac, J.-N. Rouzaud, and T. Pino. Nanostructuring of carbonaceous dust as seen through the positions of the 6.2 and 7.7 μm AIBs. *Astron. Astrophys.*, 548:A40, 2012.
- [15] M. P. Bernstein, S. A. Sandford, L. J. Allamandola, S. Chang, and M. A. Scharberg. Organic Compounds Produced by Photolysis of Realistic Interstellar and Cometary Ice Analogs Containing Methanol. *Astrophys. J.*, 454:327–344, 1995.
- [16] L. B. d’Hendecourt, L. J. Allamandola, Grim. R. J. A., and J. M. Greenberg. Time-dependent chemistry in dense molecular clouds. II - Ultraviolet photoprocessing and infrared spectroscopy of grain mantles. *Astron. Astrophys.*, 158:119–134, 1986.
- [17] A. Schriver, L. Schriver-Mazzuoli, P. Ehrenfreund, and L. d’Hendecourt. One possible origin of ethanol in interstellar medium: Photochemistry of mixed CO_2 - C_2H_6 films at 11 K. A FTIR study. *Chem. Phys.*, 334:128–137, 2007.
- [18] E. L. Gibb, D. C. B. Whittet, W. A. Schutte, A. C. A. Boogert, J. E. Chiar, P. Ehrenfreund, P. A. Gerakined, J. V. Keane, A. G. G. M. Tielens, E. F. van Dishoeck, and O. Kerhof. An inventory of interstellar ices toward the embedded protostar W33A. *Astrophys. J.*, 536:347–356, 2000.
- [19] H. W. Kroto, J. R. Heath, S. C. O. O’Brien, R. F. Curl, and R. E. Smalley. C_{60} : Buckminsterfullerene. *Nature*, 318:162–163, 1985.
- [20] S. Viti and D. A. Williams. Time-dependent evaporation of icy mantles in hot cores. *Mon. Not. R. Astron. Soc.*, 305:755–762, 1999.

- [21] S. Viti, M. P. Collings, J. W. Dever, M. R. S. McCoustra, and D. A. Williams. Evaporation of ices near massive stars: models based on laboratory temperature programmed desorption data. *Mon. Not. R. Astron. Soc.*, 354:1141–1145, 2004.
- [22] T. Curtin. *Environmental Catalysis*, chapter Selective catalytic reduction of NO_x , pages 197–210. CRC press, Taylor & Francis Group, 2005.
- [23] D. Fowler, C. Flechard, U. Skiba, M. Coyle, and N. Cape. The atmospheric budget of oxidized nitrogen and its role in ozone formation and deposition. *New Phytol.*, 193:11–23, 1998.
- [24] C. T. Driscoll, G. B. Lawrence, A. J. Bulger, T. J. Butler, C. S. Cronan, C. Eagar, K. F. Lambert, G. E. Likens, J. L. Stoddard, and K. C. Weathers. Acidic Deposition in the Northeastern United States: Sources and Inputs, Ecosystem Effects, and Management Strategies. *BioScience*, 51:180–198, 2001.
- [25] Joshua Miller. Nationwide emissions standards for diesel HDVs. *U.S. pat.*, 6962651, 2014.
- [26] Regulation (ec) no 595/2009 of the european parliament and of the council. *Official Journal of the European Union*, L 188:1–13, 2009.
- [27] T. V. Johnson. Review of diesel emissions and control. *Int. J. Engine Res.*, 10:275–285, 2009.
- [28] I. A. Resitoglu, K. Altinisik, and A. Keskin. The pollutant emissions from diesel-engine vehicles and exhaust aftertreatment systems. *Clean Technol. Environ. Policy*, 17:15–27, 2015.
- [29] A. M Beale, F. Gao, I. Lezcano-Gonzalez, C. H. F. Peden, and J. Szanyi. Recent Advances in Automotive Catalysis for NO_x Emission Control by Small-Pore Microporous Materials. *Chem. Soc. Rev.*, 44:7371–7405, 2015.
- [30] R. A. van Santen and J. W. Niemantsverdriet, editors. *Chemical Kinetics and Catalysis*. Springer, 1995.
- [31] Andrew Zangwill. *Physics at Surfaces*. Cambridge University Press, 1996.
- [32] M. Bowker and D. A. King. Adsorbate diffusion on single crystal surfaces. *Surf. Sci.*, 71:583–598, 1978.
- [33] M. P. Collings, M. A. Anderson, R. Chen, J. W. Dever, S. Viti, D. A. Williams, and M. R. S. McCoustra. A laboratory survey of the thermal desorption of astrophysically relevant molecules. *Mon. Not. R. Astron. Soc.*, 354:1133–1140, 2004.

- [34] S. E. Bisschop, H. J. Fraser, K. I. Öberg, E. F. van Dishoeck, and S. Schlemmer. Desorption rates and sticking coefficients for CO and N₂ interstellar ices. *Astron. Astrophys.*, 449:1297–1309, 2006.
- [35] K. I. Öberg, F. van Broekhuizen, H. J. Fraser, S. E. Bisschop, E. F. van Dishoeck, and S. Schlemmer. Competition between CO and N₂ Desorption from Interstellar Ices. *Astrophys. J., Lett.*, 621:L33–L36, 2005.
- [36] H. J. Fraser, M. P. Collings, M. R. S. McCoustra, and D. A. Williams. Thermal desorption of water ice in the interstellar medium. *Mon. Not. R. Astron. Soc.*, 327:1165–1172, 2001.
- [37] D. Laufer, E. Kochavi, and A. Bar-Nun. Structure and dynamics of amorphous water ice. *Phys. Rev. B*, 36:9219–9227, 1987.
- [38] R. S. Smith, N. G. Petrik, G. A. Kimmel, and B. D. Kay. Thermal and Nonthermal Physiochemical Processes in Nanoscale Films of Amorphous Solid Water. *Acc. Chem. Res.*, 45:33–42, May 2011.
- [39] W. A. Brown, S. Viti, A. J. Wolff, and A. S. Bolina. Laboratory investigations of the role of the grain surface in astrochemical models. *Faraday Discuss.*, 133:113–124, 2006.
- [40] A. S. Bolina, A. J. Wolff, and W. A. Brown. Reflection Absorption Infrared Spectroscopy and Temperature-Programmed Desorption Studies of the Adsorption and Desorption of Amorphous and Crystalline Water on a Graphite Surface. *J. Phys. Chem. B*, 109:16836–16845, 2005.
- [41] A. S. Bolina, A. J. Wolff, and W. A. Brown. Reflection absorption infrared spectroscopy and temperature programmed desorption investigations of the interaction of methanol with a graphite surface. *J. Chem. Phys.*, 122:044713–12, 2005.
- [42] W. A. Brown and A. S. Bolina. Fundamental data on the desorption of pure interstellar ices. *Mon. Not. R. Astron. Soc.*, 374:1006–1014, 2007.
- [43] D. Chakarov, L. Österlund, and B. Kasemo. Water adsorption on graphite (0001). *Vacuum*, 46:1109–1112, 1995.
- [44] D. Chakarov, L. Österlund, and B. Kasemo. Water Adsorption and Coadsorption with Potassium on Graphite(0001). *Langmuir*, 11:1201–1214, 1995.
- [45] J. D. Thrower, M. P. Collings, F. J. M Rutten, and M. R. S. McCoustra. Laboratory investigations of the interaction between benzene and bare silicate grain surfaces. *Mon. Not. R. Astron. Soc.*, 394:1510–1518, 2009.

- [46] J. A. Noble, E. Congiu, F. Dulieu, and H. J. Fraser. Thermal desorption characteristics of CO, O₂ and CO₂ on non-porous water, crystalline water and silicate surfaces at submonolayer and multilayer coverages. *Mon. Not. R. Astron. Soc.*, 421:768–779, 2012.
- [47] M. N. Mautner, V. Abdelsayed, M. S. El-Shall, J. D. Throver, S. D. Green, M. P. Collings, and M. R. S. McCoustra. Meteorite nanoparticles as models for interstellar grains: Synthesis and preliminary characterisation. *Faraday Discuss.*, 133:103–112, 2006.
- [48] P. Delhaés. *Graphite and Precursors*. Gordon and Breach Science Publishers, 2001.
- [49] K. S. Novoselov, A. K. Geim, S. V. Morozov, D. Jiang, Y. Zhang, S. V. Dubonos, I. V. Grigorieva, and A. A. Firsov. Electric Field Effect in Atomically Thin Carbon Films. *Science*, 22:666–669, 2004.
- [50] D. Chakarov and B. Kasemo. Photoinduced Crystallization of Amorphous Ice Films on Graphite. *Phys. Rev. Lett.*, 81(23):5181–5184, December 1998.
- [51] P. Löfgren, P. Ahlström, D. Chakarov, J. Lausmaa, and B. Kasemo. Substrate dependent sublimation kinetics of mesoscopic ice films. *Surf. Sci.*, 367:L19–L25, 1996.
- [52] A. D. McNaught and A. Wilkinson. *IUPAC. Compendium of Chemical Terminology*. Blackwell Scientific Publications, Oxford, 2nd edition, 1997.
- [53] H. Fredriksson, Y. Alaverdyan, A. Dmitriev, C. Langhammer, D. S. Sutherland, M. Zäch, and B. Kasemo. Hole-mask colloidal lithography. *Adv. Mater.*, 19:4297–4302, 2007.
- [54] H. Fredriksson, T. Pakizeh, M. Käll, B. Kasemo, and D. Chakarov. Resonant optical absorption in graphite nanostructures. *J. Opt. A: Pure Appl. Opt.*, 11:114022, 2009.
- [55] Y. Maréchal. *The Hydrogen Bond and the Water Molecule*. Elsevier, 2007.
- [56] D. Eisenberg and W. Kauzmann. *The structure and properties of water*. Oxford University Press, 1969.
- [57] M. Kleman and O. D. Lavrentovich. *Soft Matter Physics: An Introduction*. Springer-Verlag, New York, 2003.
- [58] P. Jenniskens and D. F. Blake. Structural Transitions in Amorphous Water Ice and Astrophysical Implications. *Science*, 265:753, 1994.

- [59] R. S. Smith, C. Huang, E. K. L. Wong, and B. D. Kay. Desorption and crystallization kinetics in nanoscale thin films of amorphous water ice. *Surf. Sci.*, 367:L13, 1996.
- [60] K. P. Stevenson, G. A. Kimmel, Z. Dohnalek, R. S. Smith, and B. D. Kay. Controlling the Morphology of Amorphous Solid Water. *Science*, 283:1505, 1999.
- [61] Y. Handa and D. D. Klug. Heat capacity and glass transition behavior of amorphous ices. *J. Phys. Chem.*, 92:3323, 1988.
- [62] A. Hallbrucker, E. Mayer, and G. P. Johari. Glass-liquid transition and the enthalpy of devitrification of annealed vapor-deposited amorphous solid water. A comparison with hyperquenched glassy water. *J. Phys. Chem.*, 93:4986, 1989.
- [63] P. Löfgren, P. Ahlström, J. Lausma, B. Kasemo, and D. Chakarov. Crystallization Kinetics of Thin Amorphous Water Films on Surfaces. *Langmuir*, 19:265–274, 2003.
- [64] N. J. Sack and R. A. Baragiola. Sublimation of vapor-deposited water ice below 170 k, and its dependence on growth conditions. *Phys. Rev. B*, 48:9973, 1993.
- [65] R. B. Phelps, L. L. Kesmodel, and R. J. Kelly. Adsorption of H₂O on Bi₂Sr₂CaCu₂O₈ and graphite studied with HREELS. *Surf. Sci.*, 340:134–140, 1995.
- [66] P. Cabrera Sanfeliix, S. Holloway, K. W. Kolasinski, and G. R. Darling. The structure of water on the (0 0 0 1) surface of graphite. *Surf. Sci.*, 532-535:166–172, 2003.
- [67] A. Ambrosetti, F. Ancilotto, and P. L. Silvestrelli. van der Waals-Corrected Ab Initio Study of Water Ice-Graphite Interaction. *J. Phys. Chem. C*, 117:321–325, 2013.
- [68] M. S. Dresselhaus and G. Dresselhaus. Intercalation compounds of graphite. *Adv. Phys.*, 30:139–326, 1981.
- [69] S. Sircar and A. L. Myers. *Handbook of Zeolite Science and Technology*, chapter Gas Separation by Zeolites. CRC Press, 2003.
- [70] S. Kulprathipanja, editor. *Zeolites in Industrial Separation and Catalysis*. Wiley-VCH, 2010.
- [71] T. De Baerdemaeker and D. De Vos. Trapdoors in zeolites. *Nat. Chem.*, 5:89–90, 2013.

- [72] A. Zatta, R. Clerici, E. Faccetti, P. Mattioli, M. R. Rabaioli, P. Radici, R. Aiello, and F. Crea. Zeolite AX - a new zeolite builder for detergents. *Jornadas - Comité español de la detergencia*, 27:25, 1998.
- [73] R. J. Taylor and R. H. Petty. Selective hydroisomerization of long chain normal paraffins. *Appl. Catal., A*, 119:121–138, 1994.
- [74] S. Miller and J. Rosenbaum. Method for producing a plurality of lubricant base oils from paraffinic feedstock. *U.S. pat.*, page No. 6962651, 2005.
- [75] J. Čejka, A. Corma, and S. Zones, editors. *Zeolites and Catalysis*. Wiley-VCH, 2010.
- [76] J. Jansson. *Urea-SCR Technology for deNO_x After Treatment of Diesel Exhausts*, chapter 3, pages 65–69. Springer Science and Business Media, New York, 2014.
- [77] J. W. Byrne, J. M. Chen, and B. K. Speronello. Selective catalytic reduction of NO, using zeolitic catalysts for high temperature applications. *Catal. Today*, 13:33–42, 1992.
- [78] K. C. C. Kharas, D. J. Liu, and H. J. Robota. Structure-function properties in cu-ZSM-5 NO decomposition and NO SCR catalysts. *Catal. Today*, 26:129–145, 1995.
- [79] B. Coq, M. Mauvezin, G. Delahay, J. B. Butet, and S. Kieger. The simultaneous catalytic reduction of no and N₂O by NH₃ using an fe-zeolite-beta catalyst. *Appl. Catal. B*, 27:193–198, 2000.
- [80] A. M. Frey, S. Mert, J. Due-Hansen, R. Fehrmann, and C. H. Christensen. Fe-BEA Zeolite Catalysts for NH₃-SCR of NO_x. *Catal. Lett.*, 130:928–935, 2009.
- [81] J. H. Kwak, R. G. Tonkyn, D. H. Kim, J. Szanyi, and C. H. F. Peden. Excellent activity and selectivity of cu-SSZ-13 in the selective catalytic reduction of NO_x with NH₃. *J. Catal.*, 275:187–190, 2010.
- [82] D. W. Fickel, E. D’Addio, J. A. Lauterbach, and R. F. Lobo. The ammonia selective catalytic reduction activity of copper-exchanged small-pore zeolites. *Appl. Catal. B*, 102:441–448, 2011.
- [83] J. Andersen, J. E. Bailie, J. L. Casci, H. Y. Chen, J. M. Fedeyko, and R. K. S. Foo. Transition Metal/Zeolite SCR Catalysts. *WO pat.*, WO/2008/132452, 2008.
- [84] I. Bull, W. M. Xue, P. Burk, R. S. Boorse, W. M. Jaglowski, G. S. Koermer, A. Moini, J. A. Patchett, J. C. Dettling, and M. T. Caudle. Copper CHA Zeolite Catalysts. *U.S. pat.*, 7601662B2, 2009.

- [85] I. Bull, A. Mioni, G. S. Koermer, J. A. Patchett, W. M. Jaglowski, and S. Roth. Zeolite Catalyst with Improved NO_x Reduction in SCR. *U.S. pat.*, 7704475B2, 2010.
- [86] J. Andersen, H. Y. Chen, J. M. Fedeyko, and E. Weigert. Small Pore Molecular Sieve Supported Copper Catalysts Durable against Lean/Rich Aging for the Reduction of Nitrogen Oxides. *U.S. pat.*, 7998443B2, 2011.
- [87] D. W. Fickel and R. F. Lobo. Copper Coordination in Cu-SSZ-13 and Cu-SSZ-16 Investigated by Variable-Temperature XRD. *J. Phys. Chem. C*, 114:1633–1640, 2010.
- [88] S. T. Korhonen, D. W. Fickel, R. F. Lobo, B. M. Weckhuysen, and A. M. Beale. Isolated Cu²⁺ ions: active sites for selective catalytic reduction of NO. *Chem. Commun.*, 47:800–802, 2011.
- [89] H. G. Karge and H. K. Beyer. *Post-Synthesis Modification I, Molecular Sieves, Vol. 3*, chapter Solid-State Ion Exchange in Microporous and Mesoporous Materials, pages 47–201. Springer-Verlag, Berlin Heidelberg, 2002.
- [90] S. Shwan, M. Skoglundh, L. F. Lundegaard, R. R. Tiruvalam, T. V. W. Janssens, A. Carlsson, and P. N. R. Vennestrom. Solid-state ion-exchange of copper into zeolites facilitated by ammonia at low temperature. *ACS Catal.*, 5:16–19, 2015.
- [91] F. Gao, E. D. Walter, E. M. Karp, J. Luo, R. G. Tonkyn, J. H. Kwak, J. Szanyi, and C. H. F. Peden. Structure-activity relationships in NH₃-SCR over Cu-SSZ-13 as probed by reaction kinetics and EPR studies. *J. Catal.*, 300:20–29, 2013.
- [92] U. Deka, A. Juhin, E. A. Eilertsen, H. Emerich, M. A. Green, S. T. Korhonen, B. M. Weckhuysen, and A. M. Beale. Confirmation of Isolated Cu²⁺ in SSZ-13 Zeolite as Active Sites in NH₃-Selective Catalytic Reduction. *J. Phys. Chem. C*, 116:4809–4818, 2012.
- [93] F. Giordanino, P. N. R. Vennestrom, L. F. Lundegaard, F. N. Stappen, S. Mossin, P. Beato, S. Bordigo, and C. Lamberti. Characterization of Cu-exchanged SSZ-13: a comparative FTIR, UV-Vis, and EPR study with Cu-ZSM-5 and Cu-β with similar Si/Al and Cu/Al ratios. *Dalton Trans.*, 42:12741–12761, 2013.
- [94] S. A. Bates, A. A. Verma, C. Paolucci, A. A. Parekh, T. Anggara, A. Yezereets, W. F. Schneider, J. T. Miller, W. N. Delgass, and F. H. Ribeiro. Identification of the active Cu site in standard selective catalytic reduction with ammonia on Cu-SSZ-13. *J. Catal.*, 312:87–97, 2014.

- [95] J. H. Kwak, H. Zhu, J. H. Lee, C. H. F. Peden, and J. Szanyi. Two different cationic positions in Cu-SSZ-13? *Chem. Commun.*, 48:4758–4760, 2012.
- [96] J. H. Kwak, J. H. Lee, S. D. Burton, A. S. Lipton, C. H. F. Peden, and J. Szanyi. A Common Intermediate for N₂ Formation in Enzymes and Zeolites: Side-On Cu-Nitrosyl Complexes. *Angew. Chem., Int. Ed.*, 52:9985–9989, 2013.
- [97] F. Göttl and J. Hafner. Structure and properties of metal-exchanged zeolites studied using gradient-corrected and hybrid functionals. i. structure and energetics. *J. Chem. Phys.*, 136:064501, 2012.
- [98] F. Göttl, R. E. Bulo, J. Hafner, and P. Sautet. What Maked Copper-Exchanged SSZ-13 Zeolite Efficient at Cleaning Car Exhaust Gases? *J. Phys. Chem. Lett.*, 4:2244–2249, 2013.
- [99] J. H. Kwak, T. Varga, C. H. F. Peden, F. Gao, J. C. Hanson, and J. Szanyi. Following the movement of Cu ions in a ssz-13 zeolite during dehydration, reduction and adsorption: A combined *in situ* TP-XRD, XANES/DRIFTS study. *J. Catal.*, 314:83–93, 2014.
- [100] E. Borfecchia, K. A. Lomachenko, F. Giordanino, H. Falsig, P. Beato, A. V. Soldatov, S. Bordiga, and C. Lamberti. Revisiting the nature of Cu sites in the activated cu-SSZ-13 catalyst for SCR reaction. *Chem. Sci.*, 6:548–563, 2015.
- [101] C. W. Andersen, M. Bremholm, P. N. R. Vennestrøm, A. B. Blichfeld, L. F. Lundegaard, and B. B. Iversen. Location of Cu²⁺ in CHA zeolite investigated by X-ray diffraction using the Rietveld/maximum entropy method. *IUCrJ*, 1:382–386, 2014.
- [102] I. Lezcano-Gonzalez, U. Deka, B. Arstad, A. Van Yperen-De Deyne, K. Hemelsoet, M. Waroquier, V. Van Spreybroeck, B. M. Weckhuysen, and A. M. Beale. Determining the storage, availability and reactivity of NH₃ within cu-Chabazite-based Ammonia Selective Catalytic Reduction systems. *Phys. Chem. Chem. Phys.*, 16:1639, 2014.
- [103] F. Giordanino, E. Borfecchia, K. A. Lomachenko, A. Lazzarini, G. Agostini, E. Gallo, A. V. Soldatov, P. Beato, S. Bordiga, and C. Lamberti. Interaction of NH₃ with Cu-SSZ-13 Catalyst: A Complimentary FTIR, XANES, and XES Study. *J. Phys. Chem. Lett.*, 5:1552–1559, 2014.
- [104] V. F. Kispersky, A. J. Kropf, F. H. Ribeiro, and J. T. Miller. Low absorption vitreous carbon reactors for *operando* XAS: a case study on Cu/Zeolites for selective catalytic reduction of NO_x by NH₃. *Phys. Chem. Chem. Phys.*, 14:2229–2238, 2012.

- [105] C. Paolucci, A. A. Verma, S. A. Bates, V. F. Kispersky, J. T. Miller, R. Gounder, W. N. Delgass, F. H. Riberio, and W. F. Schneider. Isolation of the Copper Redox Steps in the Standard Selective Catalytic Reduction on Cu-SSZ-13. *Angew. Chem., Int. Ed.*, 53:11828–11833, 2014.
- [106] J.-S. McEwen, T. Anggara, W. F. Schneider, V. F. Kispersky, J. T. Miller, W. N. Delgass, and F. H. Ribeiro. Integrated *operando* X-ray absorption and DFT characterization of Cu-SSZ-13 exchange sites during the selective catalytic reduction of NO_x with NH_3 . *Catal. Today*, 184:129–144, 2012.
- [107] J. Szanyi, J. H. Kwak, H. Zhu, and C. H. F. Peden. Characterization of Cu-SSZ-13 NH_3 -SCR catalysts: an *in situ* FTIR study. *Phys. Chem. Chem. Phys.*, 15:2386, 2013.
- [108] F. Gao, E. D. Walter, M. Kollar, Y. Wang, J. Szanyi, and C. H. F. Peden. Understanding ammonia selective catalytic reduction kinetics over Cu/SSZ-13 from motion of the Cu ions. *J. Catal.*, 319:1–14, 2014.
- [109] T. V. W. Janssens, H. Falsig, L. F. Lundegaard, P. N. R. Vennestrøm, S. B. Rasmussen, P. G. Moses, F. Giordano, E. Borfecchia, K. A. Lomachenko, C. Lamberti, S. Bordiga, A. Godiksen, S. Mossin, and P. Beato. A Consistent Reaction Scheme for the Selective Catalytic Reduction of Nitrogen Oxides with Ammonia. *ACS Catal.*, 5:2832–2845, 2015.
- [110] X. Yang, Z. Wu, M. Moses-Debusk, D. R. Mullins, S. M. Mahurin, R. A. Geiger, M. Kidder, and C. K. Narula. Heterometal Incorporation in Metal-Exchanged Zeolites Enables Low-Temperature Catalytic Activity of NO_x Reduction. *J. Phys. Chem. C*, 116:23322–23331, 2012.
- [111] R. Zhang, Y. Li, and T. Zhen. Ammonia selective catalytic reduction of NO over Fe/Cu-SSZ-13. *RSC Adv.*, 4:52130–52139, 2014.
- [112] P. Sjövall. *Adsorption, desorption and reaction of oxygen containing molecules on clean and potassium covered carbon surfaces*. PhD thesis, Chalmers University of Technology, Sweden, 1992.
- [113] B. Helling, D. Chakarov, L. Österlund, V. P. Zhdanov, and B. Kasemo. Photoinduced Desorption of Potassium Atoms from a Two Dimensional Overlayer on Graphite. *J. Chem. Phys.*, 106:982, 1997.
- [114] L. E. Smart and E. A. Moore. *Solid State Chemistry*. Taylor & Francis, 2005.
- [115] J. Goldstein, D. E. Newbury, D. C. Joy, C. E. Lyman, Echlin P., E. Lifshin, L. Sawyer, and J. R. Michael, editors. *Scanning Electron Microscopy and X-ray Microanalysis*. Springer, 2003.

- [116] D. B. Williams and C. B. Carter, editors. *Transmission Electron Microscopy*. Springer, 2003.
- [117] P. Eaton and P. West, editors. *Atomic Force Microscopy*. Oxford University Press, 2010.
- [118] A. K. S. Clemens, A. Shishkin, P.-A. Carlsson, M. Skoglundh, F. J. Martínez-Casado, Z. Matej, O. Balmes, and Härelind. Reaction-driven Ion-Exchange of Copper into Zeolite SSZ-13. *ACS Catal.*, doi: 10.1021/acscatal.5b01200, 2015.
- [119] V. S. Saakov, V. Z. Drapkin, A. I. Krivchenko, E. V. Rozengart, Y. V. Bogachev, and M. N. Knyazev. *Derivative Spectrophotometry and Electron Spin Resonance (ESR) Spectroscopy for Ecological and Biological Questions*. Springer Vienna, 2013.
- [120] J. W. Niemantsverdriet, editor. *Spectroscopy in Catalysis*. Wiley-VCH, 2007.
- [121] M. Che and J. C. Védrine, editors. *Characterization of Solid Materials and Heterogeneous Catalysis*. Wiley-VCH, 2012.
- [122] S. Svanberg. *Atomic and Molecular Spectroscopy*. Springer, 2003.
- [123] I. Horcas, R. Fernández, J. M. Gómez-Rodríguez, J. Colchero, and J. Gómez-Herrero. WSXM: A software for scanning probe microscopy and a tool for nanotechnology. *Rev. Sci. Instrum.*, 78:013705, 2007.
- [124] Z. Dohnálek, G. A. Kimmel, P. Ayotte, R. Scott Smitt, and B. D. Kay. The deposition angle-dependent density of amorphous solid water films. *J. Chem. Phys.*, 118:364–372, 2003.
- [125] D. E. Brown, S. M. George, C. Huang, E. K. L Wong, K. B. Rider, R. S. Smith, and B. D. Kay. H₂O Condensation Coefficient and Refractive Index for Vapour-Deposited Ice from Molecular Beam and Optical Interference Measurements. *J. Phys. Chem.*, 100:4988–4995, 1996.
- [126] F. Göttl, P. Sautet, and I. Hermans. Can Dynamics Be Responsible for the Complex Multipeak Infrared Spectra of NO Adsorbed to Copper(ii) Sites in Zeolites? *Angew. Chem., Int. Ed.*, 54:7799–7804, 2015.
- [127] R. Zhang, J.-S. McEwen, M. Kollár, F. Gao, Y. Wang, J. Szanyi, and C. H. F. Peden. NO Chemisorption on Cu/SSZ-13: A Comparative Study from Infrared Spectroscopy and DFT Calculations. *ACS Catal.*, 4:4093–4105, 2014.

